Lund University,
Faculty of Engineering
&
School of Electronic Engineering and Computer Science
Queen Mary University of London

Master's Thesis

MODELLING GRAPHENE FIELD-EFFECT TRANSISTORS

December 19, 2017

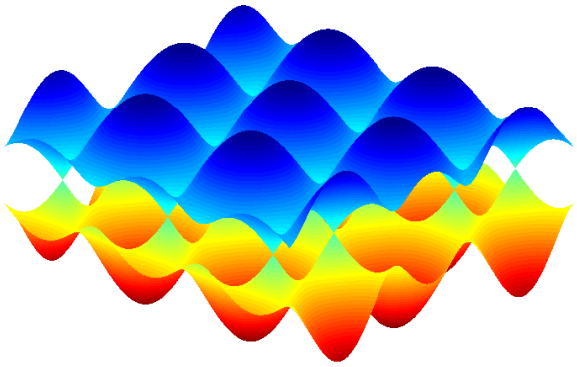

Supervisors:
Yang Hao
Jing Tian
Erik Lind

Author:
Sofia Sjölander

Examiner:
Mats Gustafsson

Abstract

Today, transistors with 20 nanometer (nm) channel length are in mass production and many researchers believe that we are reaching a limit with downsizing conventionally used silicon metal-oxide-semiconductor field-effect transistors (MOSFETs) [1]. To keep up with the trend of making the transistor smaller, new channel materials are studied, and graphene has come into the spotlight. Graphene became a serious contender mostly due to its high mobility, but other properties such as high velocity saturation and the two-dimensional (2D) nature of the material have gained more attention in recent years [2–4].

The first graphene field-effect transistor (GFET) was reported in 2004, since many transistors with graphene as a channel material have been successfully fabricated [3]. It is important to have accurate simulation models that showcase all the peculiar behaviours of GFETs. Even though several new models with high accuracy, have been presented in recent years, few theoretical explanations exist. This thesis work focuses greatly on the theory behind two different simulation models for GFETs. Several parameter approximations are investigated, with focus on the possibility of showcasing negative differential resistance (NDR).

In conclusion, we can see that the drift-diffusion (DD) model show good agreement with data and showcases NDR, while the virtual source (VS) model is more unstable and does not give NDR. I hope this thesis can act as a knowledge base, to facilitate for future simulation models.

Populärvetenskaplig sammanfattning

Transistor av materialet grafen

En av världens största uppfinningar är också den minsta av dom alla. Transistorn storlek är endast 1/5000 av ett hårstrå. Men låt inte detta lura er, tack vare denna smarta uppfinning utför din mobil mer och mer avancerade uppgifter.

Transistorn sägs vara en av de största uppfinningarna i modern historia. Uppfinningen har nämnts i samma klass som bilen och telefonen. Idag finns transistorn i nästan all modern elektronik, vilket inte är så chockerande då 2 913 276 327 576 980 000 000 stycken transistorer har tillverkats industriellt sedan 1947 [5]. Siffran blir inte mer greppbar bara för att man ser hur många transistorer det är per person på jorden; 388 436 843 677 stycken transistorer per person.

Trots detta, är inte transistorn något som diskuteras i vardagliga sammanhang. Så vad är en transistor? Enkelt uttryckt så är det en elektronikkomponent, som kan efterliknas vid en ventil. Vanligtvis har transistorn tre terminaler, vid varje terminal kan spänningen regleras. Beroende på spänningsstyrkorna ändras strömsignalen genom komponenten.

Har du märkt att våra tv-apparater, datorer och telefoner tycks bli mindre, lättare och smidigare trots att de har högre prestanda, kan lagra mer information och arbetar snabbare? Detta är till stor del tack vare utvecklingen av transistorerna. Idag finns det transistorer så små som 20 nanometer (nm) i massproduktion [3]. Okej, tänker du då, hur stort är 20 nm? Det är en mycket bra fråga, som inte är helt enkel att svara på. Generellt brukar man säga att ett hårstrå på ditt huvud är 0.1 mm, det betyder att 20 nm endast är 1/5000 av ett hårstrå. Transistorerna vi tillverkar idag är med andra ord otroligt små.

De flesta transistorer som används idag görs av Kisel. Men när dessa ska

tillverkas så små som 20 nm börjar det bli problem med materialet Kisel. Det blir läckage och oönskade kapacitanser som gör att mer energi krävs för att få önskad effekt. Forskare behövde därför fundera på om det är möjligt att byta ut Kisel mot något bättre material. Materialet grafen kom upp som tänkbar ersättare. Grafen är gjort av Kol-atomer och är ett otroligt starkt material. Materialet är dessutom bättre än någon metall på att leda ström.

I denna rapport tittar jag närmare på speciella egenskaper hos grafen. Jag går sedan vidare till teorin bakom grafen-transistorer, här beskriver jag vad som händer när man ändrar spänningen vid de olika terminalerna. Jag har skapat visuella bilder för att se vad som händer inne i transistorn. Till sist, beskriver jag hur man kan skapa en matematisk modell som beskriver strömmen som går genom grafen-transistorn.

Målet med mitt arbete var att på ett grundläggande sätt förklara teorin bakom de matematiska modellerna för grafen-transistorer. Ofta måste förenklingar göras då det är svårt att beskriva allt i en transistor matematiskt. Jag har undersökt vad tidigare forskare har gjort och jämfört olika förenklingar samt hur dessa påverkar strömsignalen.

Preface

This master thesis was carried out at Queen Mary University of London (QMUL) in London, United Kingdom. It was a final project to finish my Master of Science in Engineering Nanoscience with focus on high speed devices and nanoelectronics.

Firstly, I would like to thank Prof. Mats Gustafsson who introduced me to the interesting field of antennas and helped me get in contact with the right person at QMUL. A big thank you to Prof. Yang Hao, who welcomed me with open arms to QMUL and his research group. At QMUL I would also like to express my gratitude to my supervisor Jing Tian, who was always willing to answer my questions both in person and through emails. Many invaluable discussions have taken place at QMUL, they have given me insight in the field of graphene and graphene field-effect transistors (GFETs), as well as other valuable lessons such as the difference between a scientist and an engineer.

A special thanks also goes to my supervisor Dr. Erik Lind from Lund University, Faculty of Engineering (LTH) who have been a great help not only administrative paperwork, but also with guidance and insight into the subject.

Lastly, but by no means least, thank you to my family and my partner Max.

Acronyms

Acronym	Description. Page(s)
2D	two-dimensional. i, 1, 5
ADS	Advanced Design System. 2, 38, 42, 55, 57, 59, 61
C	carbon. 4
CVD	chemical vapour deposition. 19
DD	drift-diffusion. i, 1, 42, 43, 54, 57–60, 63–65
FET	field-effect transistor. 2, 11, 20, 21, 36, 48
FOM	figure of merit. 18, 21, 22
GFET	graphene field-effect transistor. i, iv, 1, 2, 18, 23–27, 36–38, 41–43, 59, 62–65
h-BN	hexagonal boron nitride. 19
ITRS	International Technology Roadmap for Semiconductors. 18
LTH	Lund University, Faculty of Engineering. iv
MOSFET	metal-oxide-semiconductor field-effect transistor. i, 1, 23
NDR	negative differential resistance. i, 2, 18, 23, 36–39, 41, 63–65
NEMS	nano-electromechanical systems. 18
nm	nanometer. i–iii, 1, 23
QMUL	Queen Mary University of London. iv, 2
RF	radio frequency. 18, 21
Si	silicon. 18–20, 24
SiC	silicon carbide. 19
SiO_2	silicon dioxide. 24
VS	virtual source. i, 42, 59, 61, 63–65

Notations

Notation	Description. Page(s)
α	Capacitance weighting factor. 27, 45, 46, 58, 59
a_{C-C}	The carbon-carbon distance, approximately 1.42 Å [6]. 5–8, 16, 72, 74
A_v	Intrinsic voltage gain. 18, 21, 23
c	Speed of light. 9, 13–15
$C_{ox-back}$	Back-gate oxide capacitance. 27, 46, 48, 55–57
C_{ox-top}	Top-gate oxide capacitance. 27, 46, 48, 55–57, 60
C_q	Quantum capacitance. 27, 45–47, 55, 56, 64
Δ	Spatial inhomogeneity of potential. 50, 56
E	Energy. 7–9, 13, 14, 16, 67–69, 73–76
$\mathscr{E}$	Electric field. 44
E_d	Energy at Dirac point. 10, 11, 24–26, 28–31, 34, 35, 46, 48, 54
E_f	Fermi energy. 10, 11, 24–26, 28–31, 34, 35, 46, 48, 54
$\varepsilon_{ox-back}$	Back-gate oxide permittivity. 27, 56
ε_{ox-top}	Top-gate oxide permittivity. 27, 56
f_{max}	Maximum oscillation frequency. 18, 22
f_T	Cut-off frequency. 18, 22, 23
g_m	Transconductance. 21, 53
H	Hamiltonian operator. 67–69, 71–74, 76
S	Overlap integral. 68–71
h	Planck constant, $6.626 \cdot 10^{-34}$ Js [7].
h_0	Hopping integral between nearest atom neighbours, *see equation* (A.26). 7, 73, 74
h_1	Hopping integral between next-nearest atom neighbours, *see equation* (A.35). 7, 74
$\hbar$	Reduced Planck constant, $h/(2\pi)$, *see* h. 8, 9, 11, 13, 14, 16, 26, 27, 46, 48, 50, 53, 56, 57, 75, 76

Notation	Description. Page(s)
I_{ds}	Current between drain and source. 21, 34, 37–39, 42, 44, 54–59, 61, 65
k	Boltzmann constant, $1.38 \cdot 10^{-23}$ J/K, [7]. 11, 14, 26, 27, 45, 46, 48, 54, 56, 57, 60
$\boldsymbol{k}$	Wave vector, (k_x, k_y). 7–9, 13, 14, 67, 70, 72–76
k_x	Wave number in x-direction. 7, 72, 74–76
k_y	Wave number in y-direction. 7, 16, 72, 74–76
L	Transistor channel length. 1, 44, 54–56, 58–60
λ	Mean free path. 1, 16, 43
m	Mass. 9, 13, 14
n	Electron density. 10, 11, 25, 26, 38, 48, 50, 52
n_{pud}	Charge density for electron-hole puddles.. 50, 52, 55, 57–59, 62, 63
Ω	The optical phonon energy. 53
p	Hole density. 10, 11, 25, 26, 38, 48, 50, 52
Q	Transport sheet charge density. 42, 44, 48, 54–56, 58, 60, 63
q	Elementary charge. 25–27, 45, 46, 48, 50, 53, 55–58, 60
Q_{net}	Net mobile sheet charge density. 48, 49, 53
Q_t	Charge density relevant for transport. 48–50
Q_{tot}	Total charge density relevant for transport.. 50
T	Temperature in Kelvin, T=300K in all calculations. 11, 26, 27, 45, 46, 48, 54, 56, 57, 60
$t_{ox-back}$	Back-gate oxide thickness. 27, 56
t_{ox-top}	Top-gate oxide thickness. 27, 56, 60, 63
μ	Mobility. 44, 48, 50–52, 54–56, 58–60
V	Channel-to-ground potential. 27, 29, 44, 55, 56, 64
V_{ch}	Channel potential. 23, 25–31, 33–36, 38, 40, 44–48, 50, 52, 53, 55–59, 64
V_{dirac}	Gate voltage at Dirac point. 11, 24, 28, 29, 35
$V_{dirac-0}$	Gate voltage at Dirac point when $V_{ds} = 0$. 25, 29–31, 33–36
$V_{dirac-0-back}$	Back gate voltage at Dirac point when $V_{ds} = 0$ and $V_{gs-top} = 0$. 26, 37–40, 56
$V_{dirac-0-top}$	Top gate voltage at Dirac point when $V_{ds} = 0$ and $V_{gs-back} = 0$. 26, 37–40, 56, 60
v_{drift}	Drift velocity. 42, 44, 60, 61
V_{ds}	Drain-to-source potential. 24–31, 33–41, 44, 54–61, 64, 65
v_F	Fermi velocity for graphene approximately 10^6 m/s [8–10]. 8, 11, 15, 16, 26, 27, 46, 48, 50, 52–57, 59, 75, 76

Notation	Description. Page(s)
V_{fb}	Flat-band voltage. 25
V_{gs}	Gate-to-source potential. 21, 24, 27–31, 33–40, 60
$V_{gs-back}$	Back-gate-to-source potential. 24, 26, 27, 37–40, 56
V_{gs-top}	Top-gate-to-source potential. 24, 26, 27, 38, 56
V_{in}	Input potential. 21
V_{out}	Output potential. 21
v_{sat}	Velocity saturation. 44, 48, 52–54, 56, 58–60, 64
ϕ_t	The thermal voltage kT/q. 60
W	Transistor channel width. 42, 44, 54–56, 58, 61
ψ	The orbital wavefunction. 67–70, 72, 73, 75, 76

Contents

Chapter 1

Introduction

1.1 Background

In 1965, Gordon E. Moore published the paper *Cramming more components onto integrated circuits* [11]. In the paper, Moore projected that the number of transistors per integrated circuit would have an annual doubling. Moore updated his prediction in 1975, to a doubling every second year. Today, the prediction is commonly known as "Moore's law" and even though over half a century has passed, the prediction is still true [12]. Transistors with 20 nanometer (nm) channel length are in mass production and many researchers believe that we are reaching a limit with downsizing conventionally used silicon metal-oxide-semiconductor field-effect transistors (MOSFETs) [1]. To keep up with the trend of making the transistor smaller, new channel materials are studied and graphene has come into the spotlight. Graphene became a serious contender mostly due to its high mobility, but other properties such as high velocity saturation and the two-dimensional (2D) nature of the material have gained more attention in recent years [2–4].

The first graphene MOSFET was reported in 2007 [13] and since then, a number of graphene field-effect transistors (GFETs) have been fabricated [3]. Even though plenty of working transistors have been created, modeling GFETs remains complicated and complex. Several GFET models using the drift-diffusion (DD) model have been presented in the past [14–16]. These models are only valid when the channel length L is longer than the mean free path λ, otherwise short channel effects have to be taken into consideration. As the down-scaling of transistors and GFETs continues, it remains important to create accurate models that do not ignore the effects that occur in short channel devices.

1.2 Aim

As far as developing simulation models is concerned, one of the greatest challenges lies in combining high accuracy with simple mathematics, the latter to allow implementation and model understanding. To create accurate models, it is important to have good fundamental knowledge. I have experienced that there are many articles with advanced GFETs simulation models, but few that explain the particular behaviours that we see in GFETs.

Therefore, the main goal of the Master's thesis is to describe, explain, showcase along with mathematically prove the different behaviours in GFETs. I want to showcase equations as well as visual images to simplify the understanding of the complicated behaviours of GFETs. I hope to create a good basis, for someone to read who is interested in modelling GFETs.

This thesis work will then use the theory when comparing some different simulation models. I will look into how they are built and how this ties in with the theory. I aim to get an understanding of why different models give accurate and inaccurate results, as well as which approximations work and why. I will only look at models that can or have been implemented in the hardware description language Verilog-A. These models can be run with the simulation program Advanced Design System (ADS) [17]. I will use MATLAB [18] to analyse, compare and verify equations at earlier stages.

During my studies, I have always been encouraged to do background research and understand the usefulness of my work result, which is why a part of my thesis report will focus on the state of art, prospects and obstacles of graphene as well as GFETs.

My thesis work will take place at Queen Mary University of London (QMUL), in the Electronics department. At the department, a group of people are focusing on negative differential resistance (NDR) in GFETs. Therefore I will favour models that manage to showcase that particular phenomena. I will also focus on understanding the different explanations for the phenomena.

1.3 Report Structure

This report focuses greatly on the theory behind GFET. *Chapter 2 Graphene* explores graphene from the atomic to the practical scale. It is followed by *Chapter 3 Field-Effect Transistor*, that gives a general introduction to field-effect transistors (FETs). *Chapter 4 Graphene Field-Effect Transistor* and *Chapter 5 Modelling Graphene Field-Effect Transistor* both focus on GFETs, the first on the theory and visual representation to understand the transport behaviours, while the latter presents different simulation models. Finally, we conclude with

Chapter 6 Discussion of Result that discusses the different models together with an idea of what I think can be done in future work. A list of acronyms as well as notations are shown in the pre-matter, please refer back to these lists if an abbreviation is unclear.

Chapter 2

Graphene

Graphene is a fascinating material that not only conducts heat and electricity better than any other metal, but is also transparent and flexible. The material can withstand mechanical deformation and be folded without breaking. Graphene has high impermeability for gases and is chemically inert and stable. What makes graphene unique and so intriguing is that all these sought-after properties are combined into one single material [3].

In this chapter, graphene is described in depth. The chapter starts of on the atomic scale and continues to up-scale to the band structure, charge density and concludes with graphene applications.

2.1 Atomic Structure

Carbon (C) is an essential element to our existence [6]. It is the second most common element in the human body and a key component of all known life.

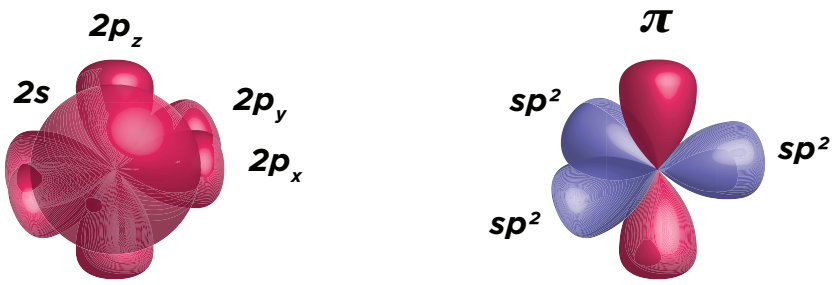

Figure 2.1: Visual representation of the orbitals in carbon (C) before and after sp^2-hybridisation.

Still, it was very recently discovered that carbon in its two-dimensional (2D) form, can be stable under ambient conditions [10].

Carbon has got four valence electrons in the $2s$, $2p_x$, $2p_y$ and $2p_z$ orbitals. Through sp^2-hybridisation, three sp^2 orbitals are created, connecting each orbital to the adjacent carbon neighbour with a strong covalent in-plane σ-bond [6, 19]. The connected carbon atoms create a single-layered honeycomb structure material known as graphene [3, 6, 20]. The last valence electron, from the $2p_z$ orbital, creates the π-orbital perpendicular to the other orbitals. The π-orbitals define the thickness and enable high conductivity in graphene [19], which is why graphene under many circumstances can be treated as a material with just one conduction electron per atom [21].

The atomic arrangement of graphene can be described as a triangular Bravais [7] lattice with a basis of two atoms per unit cell, see figure 2.2. The lattice points shown to the left in figure 2.3 can be written as

$$\begin{aligned} \boldsymbol{a}_1 &= \left(\frac{3}{2} a_{C-C},\ \frac{\sqrt{3}}{2} a_{C-C} \right), \\ \boldsymbol{a}_2 &= \left(\frac{3}{2} a_{C-C},\ -\frac{\sqrt{3}}{2} a_{C-C} \right), \end{aligned} \tag{2.1}$$

Where a_{C-C} is the carbon-carbon distance. The three nearest-neighbour vectors, to the left in figure 2.3, can be written as

$$\begin{aligned} \boldsymbol{\delta}_1 &= (a_{C-C},\ 0), \\ \boldsymbol{\delta}_2 &= \left(-\frac{1}{2} a_{C-C}, \frac{\sqrt{3}}{2} a_{C-C} \right), \\ \boldsymbol{\delta}_3 &= \left(-\frac{1}{2} a_{C-C}, -\frac{\sqrt{3}}{2} a_{C-C} \right). \end{aligned} \tag{2.2}$$

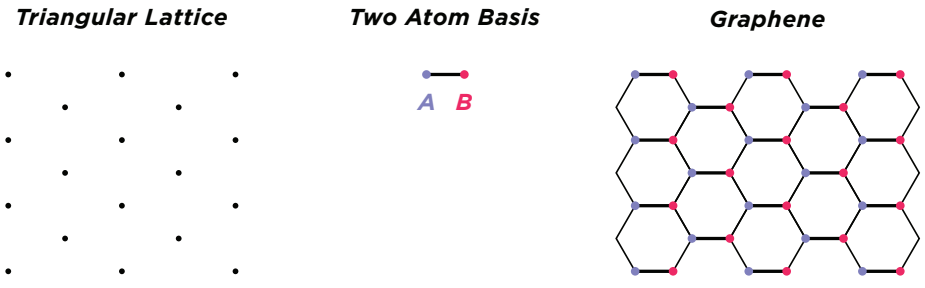

Figure 2.2: Triangular lattice structure with two atom basis gives the honeycomb structure of graphene.

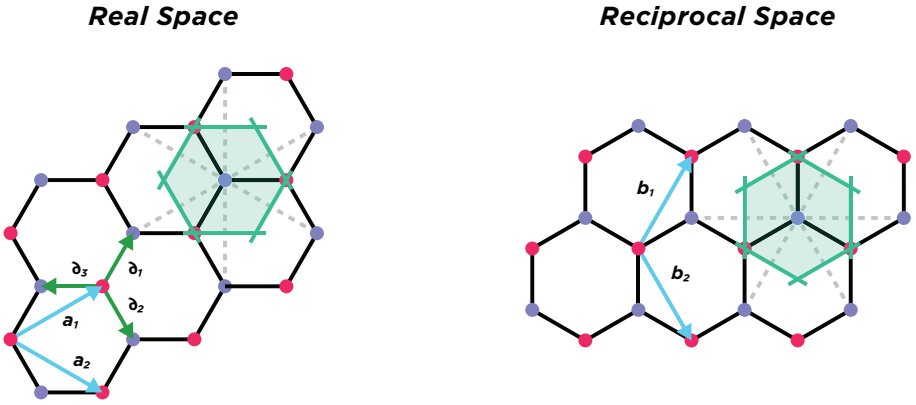

Figure 2.3: Lattice structure for graphene, in real (left) and reciprocal space (K-space) (right).

The Wigner-Seitz cell definition is typically used to describe the primitive cell in a crystal. The area of the Wigner-Seitz cell is defined as containing exactly one Bravais lattice point (in this case the basis of two atoms) as well as the area constructed by separating the bisectors in between each lattice point with perpendicular lines. The hexagonal Wigner–Seitz cell for graphene, in real space, is shown in figure 2.3 to the left.

Real space gives a good understanding of the atomic arrangement, but some aspects are difficult to showcase, therefore reciprocal space (also known as momentum space or K-space) can be used. For example, reciprocal space shows wave interactions more clearly, which is useful when working with electronic materials on a low scale [22]. After conversion, the reciprocal lattice vectors, $\boldsymbol{a}_1$ and $\boldsymbol{a}_2$ in figure 2.3, can be written as

$$\begin{aligned} \boldsymbol{b}_1 &= \left(\frac{2\pi}{3a_{C-C}}, \frac{2\pi}{\sqrt{3}a_{C-C}} \right), \\ \boldsymbol{b}_2 &= \left(\frac{2\pi}{3a_{C-C}}, -\frac{2\pi}{\sqrt{3}a_{C-C}} \right). \end{aligned} \tag{2.3}$$

The Wigner-Seitz cell in reciprocal space, commonly known as the the first Brillouin zone [6, 23], is marked to the right in figure 2.3.

2.2 Band Structure

Graphene can, as was mentioned earlier, be treated as a material containing only one conduction electron per atom [21]. Therefore, to get a better understanding of graphene, it is wise to look at the energy dispersion (band structure) of the

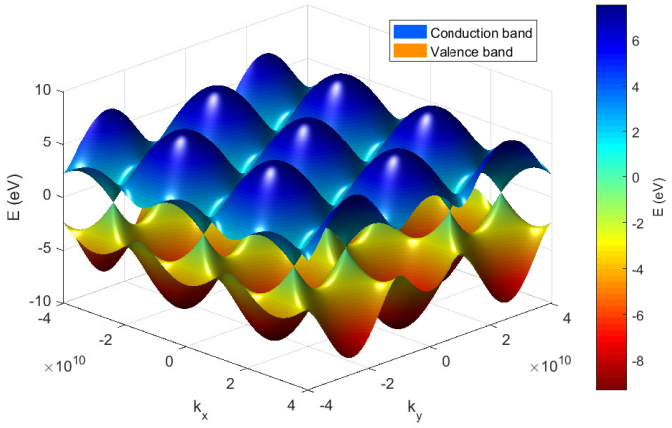

Figure 2.4: Energy dispersion in graphene as a function of k_x and k_y from equation (2.4).

electrons in the π-orbitals. The energy,

$$E_{\pm}(\boldsymbol{k}) = \pm\, h_0\sqrt{|f(\boldsymbol{k})|^2} - h_1|f(\boldsymbol{k})|^2, \tag{2.4}$$

is derived from the tight-binding Hamiltonian considering that electrons in the π-orbitals can hop to both their nearest and next-nearest neighbour atoms[1]. $|f(\boldsymbol{k}|^2$ is defined as

$$|f(\boldsymbol{k})|^2 = 3 + 4\cos\left(\frac{\sqrt{3}}{2}k_y a_{C-C}\right)\cos\left(\frac{3}{2}k_x a_{C-C}\right) + 2\cos\left(\sqrt{3}k_y a_{C-C}\right) \tag{2.5}$$

h_0 is the hopping integral between the nearest atom neighbours, while h_1 is the next-nearest neighbour hopping integral [6]. If electrons are considered to only hop to their nearest neighbour $h_1 = 0$ can be set [19]. $\boldsymbol{k}$ is the momentum vector defined as (k_x, k_y), while a_{C-C} is the carbon-carbon distance. The positive part of the energy dispersion refers to the conduction band and the negative part to the valence band. Figure 2.4 shows a visual representation of equation (2.4) as a function of momentum, k_x and k_y. The values used are [6]

$$\begin{aligned} h_0 &= 2.8 \text{ eV}, \\ h_1 &= 0.1 \text{ eV}. \end{aligned} \tag{2.6}$$

An enlargement focusing on the Brillouin zone is shown in figure 2.5. In the

[1] All calculations, assumptions and approximations are shown explicitly in *Appendix A Graphene energy dispersion using tight-binding approximation.*

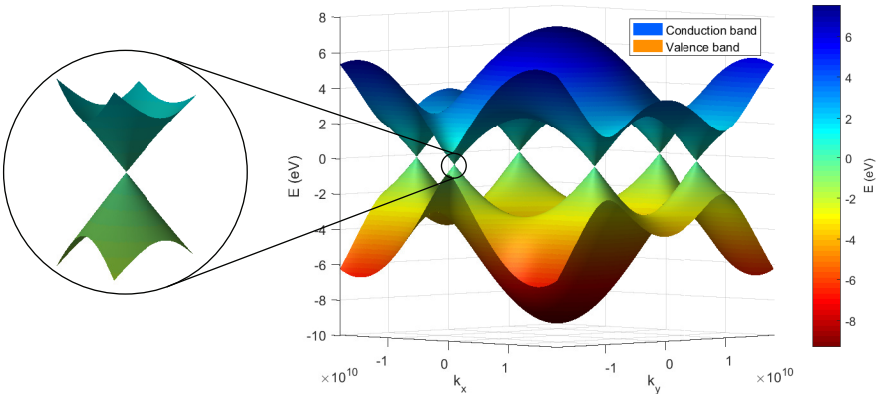

Figure 2.5: Enlargement of figure 2.4 focusing on the Brillouin zone. Circled area shows magnification at K-point.

figure, it is clear that the conduction and valence band meet at six corner points at the edge of the Brillouin zone. These conical meeting points are often referred to as the Dirac or K-points of the hexagonal Brillouin zone [6,24]. Their position, relative to the centre of the Brillouin zone, can be written as

$$\begin{aligned} K &= \left(\frac{2\pi}{3a_{C-C}}, \frac{2\pi}{3\sqrt{3}a_{C-C}} \right), \\ K' &= \left(\frac{2\pi}{3a_{C-C}}, -\frac{2\pi}{3\sqrt{3}a_{C-C}} \right). \end{aligned} \tag{2.7}$$

A magnification close to one of the Dirac points is shown to the left in figure 2.5. The magnification shows that particles in graphene exhibit linear dispersion relation close to the Dirac points as

$$E = \pm \hbar v_F |\boldsymbol{k}|, \tag{2.8}$$

where v_F is the Fermi velocity of graphene and $\hbar$ is the reduced Planck constant. The shape of the band structure, especially close to the Dirac point, is of great interest, as it does not resemble the shape of conventional metals and semiconductor materials, where the band structure is approximately parabolic near the band gap [6, 10]. Another noticeable finding is that graphene has no band gap unlike an insulator and no partly filled bands like a metal, instead the valence and conduction band meet at the Dirac points. Graphene is therefore sometimes referred to as a semi-metal [3]. See figure 2.6 for a visual comparison between the materials.

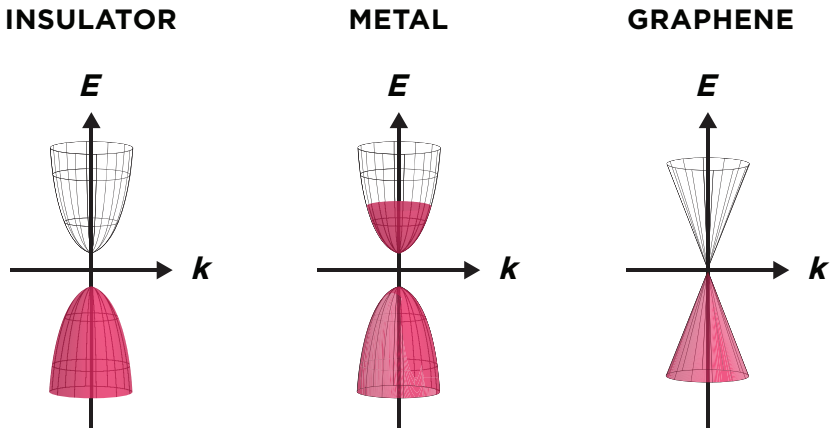

Figure 2.6: Energy dispersion for an insulator, a metal and graphene.

2.3 Anti-particles

The linear energy dispersion of graphene closely resembles the Dirac spectrum of massless Dirac particles [6]. An essential feature of the Dirac spectrum is the existence of anti-particles: electrons and positrons (fermions). For Dirac particles with mass m, there is an energy band gap between the minimal electron energy, $E_0 = mc^2$, and the maximal positron energy, $-E_0$. This means that the size of the energy band gap depends on the mass of the fermions, decreasing for particles with less mass. Far away from the band gap, the energy of the Dirac fermion depends linearly on the wave vector as

$$E = \pm\hbar c|\boldsymbol{k}|, \tag{2.9}$$

where c is the speed of light. For Dirac particles without mass the band gap is zero and the linear relation, in equation (2.9), holds at any energy [10]. This linear energy dispersion in massless Dirac fermions, is very similar to that of graphene, which is why graphene is often compared with massless Dirac fermions. It is an interesting similarity since it explains a lot of the specific characteristics in graphene, that are normally seen for Dirac particles. More specifically for graphene, this means that for any electron state with a positive energy E, a corresponding conjugated hole state with energy -E must exist. This property is often referred to as the charge-conjugation symmetry [9,10,24]. Electrons and holes in graphene are interconnected, which is rare in other commonly used materials where electrons and holes are described by separate (non-connected) Schrödinger equations [6,8].

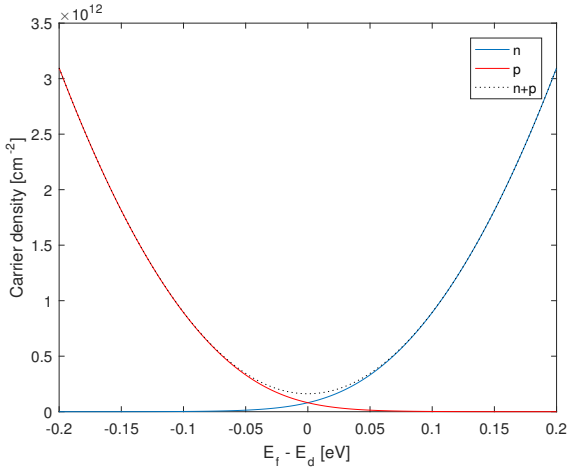

Figure 2.7: Carrier densities for electrons n and holes p, versus the difference between the Fermi level and the Dirac point $E_f - E_d$.

2.4 Local Equilibrium

Before merging further into the traits of graphene it is important to clarify some expressions. A system that does not exchange matter or heat with the surroundings, where the variables of the system are independent of time but vary with position, is said to be in non-uniform equilibrium. For a system to be in non-uniform equilibrium the electrochemical potential, also known as the Fermi level, has to be constant. If a voltage is applied over a graphene sheet the Fermi level cannot be constant and non-uniform equilibrium cannot be established. But, if in some small neighbourhood of a point one can assume that the potential is close to constant the system is said to be in local (non-uniform) equilibrium. For these local points quasi-Fermi levels can be established [25]. In this report the expression Fermi level, with the notation E_f, will be used for both Fermi levels and quasi-Fermi levels . Now that the notation of E_f has been clarified let us move on to the charge density.

2.5 Charge Density

At absolute zero temperature, in neutral and discrepancy free graphene, the valence band is completely filled and the conduction band is empty, meaning that the Fermi level E_f goes straight through the Dirac point E_d [21]. However if a potential is applied, creating an electric field, the Fermi level moves which therefore change the charge density. For electrons and holes, the charge densities

can be expressed as

$$n = \frac{2(kT)^2}{\pi(\hbar v_F)^2}\mathfrak{F}_1\left(\frac{E_f - E_d}{kT}\right), \tag{2.10}$$

$$p = \frac{2(kT)^2}{\pi(\hbar v_F)^2}\mathfrak{F}_1\left(-\frac{E_f - E_d}{kT}\right). \tag{2.11}$$

$\mathfrak{F}_1(\cdot)$ is the first-order Fermi-Dirac integral, k is Boltzmann constant and $E_f - E_d$ is the distance between the Fermi level and the Dirac point. As $|E_f - E_d|$ gets larger, the total charge density $n + p$, will increase, thereby increasing the conductivity and thus making graphene more metallic [7]. This effect is known as the electric field effect, and was shown experimentally in one of the first publications about graphene. The effect is a fundamental trait used in electronic devices, for example in field-effect transistors (FETs) [26].

Unfortunately, graphene is normally not as simple as described above. It is common that, even in unloaded graphene, due to discrepancies and imperfections as well as materials in conjunction interacting with graphene, that $E_f \neq E_d$ [6]. This means that the conductivity minimum might might occur when no potential is applied, but rather when a specific potential is applied moving the levels so that $E_f = E_d$. The potential needed is referred to as the Dirac voltage V_{dirac} [20].

2.6 Klein Tunnelling

In conventional mechanics, where particles is described as point masses, particles cannot propagate through a region where the potential energy is higher than the total energy of the particle. However, in (non-relativistic) quantum mechanics, particles are described by a probability wave from the Schrödinger equation. When a probability wave hits a potential barrier, it will go inside the barrier, contrary to conventional mechanics. The wave will decay exponentially inside the barrier, with greater damping for higher barriers. For thick and high barriers, the wave will be very dampened for a long period, so that only a tiny part or no part at all comes out on the other side of the barrier. Hence, the probability of tunnelling and the transmission coefficient will be small. However, for a thinner and lower barriers a greater part of the probability wave can penetrate, which increases the probability of tunnelling and gives a higher transmission coefficient. This phenomena, when the total energy of the particle does not exceed that of the potential barrier, but it still goes through the barrier, is known as quantum tunnelling [27].

Then again, as we have discovered electrons and holes in graphene are not described by the Schrödinger equation. So, it is intriguing to see what happens

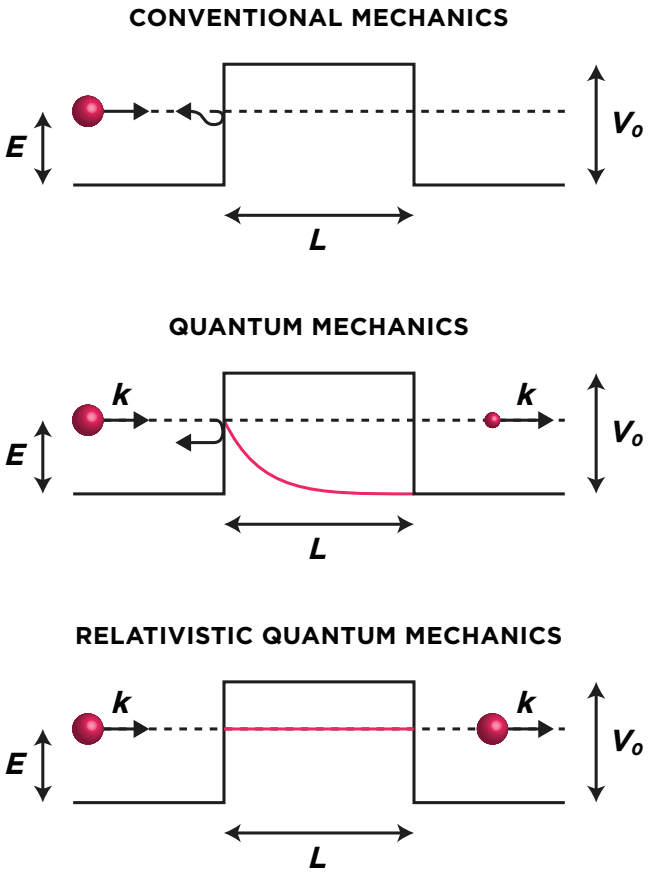

Figure 2.8: Particle travelling towards potential barrier for conventional, non-relativistic quantum and relativistic quantum particles. The size of the ball is proportional to the transmission coefficient.

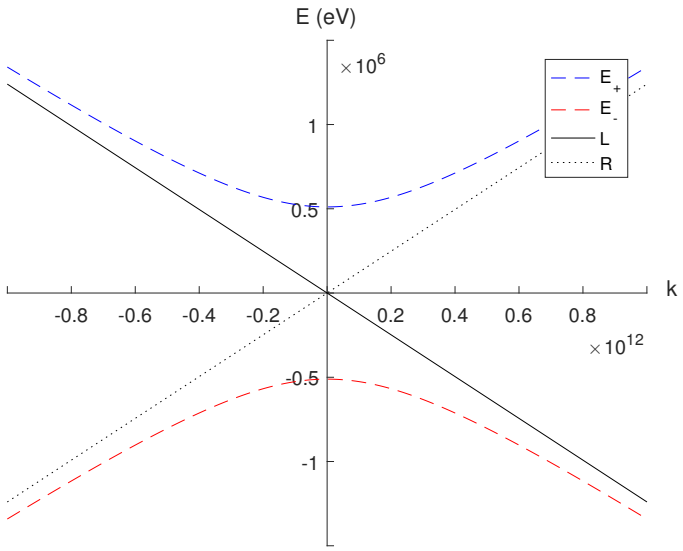

Figure 2.9: Energy dispersion for relativistic electrons from equation (2.12)*. L and R represents asymptotes and when the mass m goes to zero.*

the Dirac equation is applied to the barrier problem. To get a better understanding of the problem, let us start by looking at what happens with a single relativistic electron.

2.6.1 Single relativistic electron

The energy eigenvalues of the Dirac equation for a single relativistic electron, with mass m, can be written as

$$E = \pm\sqrt{(\hbar c\boldsymbol{k})^2 + (mc^2)^2}, \tag{2.12}$$

and is shown visually in figure 2.9. The upper branch E_+ represents the positive part of the equation and the lower branch E_- represent the negative part of the equation. From the figure it can be seen that, for real values of $\boldsymbol{k}$ we must have $E > mc^2$ or $E < -mc^2$. Let us imagine that an electron is in a positive energy state E_+ and that it is travelling in the positive x-direction as seen in figure 2.9. At some point the electron encounters a potential barrier V_0. If $E - V_0 > mc^2$ the electron will continue travelling in the positive x-direction, but with a wave number that now has to satisfy

$$E - V_0 = \sqrt{(\hbar c\boldsymbol{k})^2 + (mc^2)^2}. \tag{2.13}$$

Equation (2.13) can only be satisfied if $\boldsymbol{k}^2 > 0$, which means that $\boldsymbol{k}$ cannot be imaginary. For positive group velocity, $\boldsymbol{k}$ also has to be positive. On the other hand, if the potential very high so that $E - V_0 < -mc^2$, the wave number must satisfy

$$E - V_0 = -\sqrt{(\hbar ck)^2 + (mc^2)^2}. \tag{2.14}$$

For equation (2.14) to be satisfied $\boldsymbol{k}$ cannot be imaginary. The electron will be in the E_- branch, but for it to have a positive group velocity, $\boldsymbol{k}$ also have to be negative. This means that the particle continues to propagate in the positive x-direction with a negative $\boldsymbol{k}$-value. This is what Klein noted in his famous publication *Die Reflexion von Elektronen an einem Potentialsprung nach der relativistischen Dynamik von Dirac* from 1929 [28].

If the value of V_0 is something in between our two examples, $-mc^2 < E - V_0 < mc^2$, then the dispersion relationship in equation (2.12) can only be satisfied if $\boldsymbol{k}^2 < 0$. That means that $\boldsymbol{k}$ has to be imaginary. An imaginary wave number gives a exponential decay, just like in quantum mechanics, therefore if this condition is fulfilled, the wave will be completely or partly reflected.

Perfect transmission is accomplish if the value of V_0 goes to infinity, this is the phenomena known as Klein paradox [29]. The essence of the paradox lies in the prediction that when a relativistic quantum particle, described by the Dirac equation, travels towards a barrier, such as in figure 2.8, the barrier becomes more transparent with increased potential V_0, in contrast to a conventional non-relativistic particle, described by the Schrödinger equation, where the probability of tunnelling decreases with increased potential [8]. Even though the paradox is well accepted there are still different theoretical explanations [30]. One common and intuitive explanation is that, a strong potential is repulsive for electrons but attractive for holes, which results in holes being carriers [31].

2.6.2 Massless relativistic particle

When the mass m, in equation (2.12) and figure 2.9, goes towards zero the energy dispersion E will coincide with the two lines L and R. Particles belonging to line L have a negative group velocity, therefore travelling in the left direction, while particles on line R have a positive group velocity and will travel in the right direction. This means that there is no gap between the lowest energy of E_+ and the highest energy of E_-, hence there is no imaginary $\boldsymbol{k}$-phase where the wave can be reflected. The expression,

$$E = \pm\hbar c|\boldsymbol{k}|. \tag{2.15}$$

always holds for the massless case [29]. Once again it is noticable that equa-

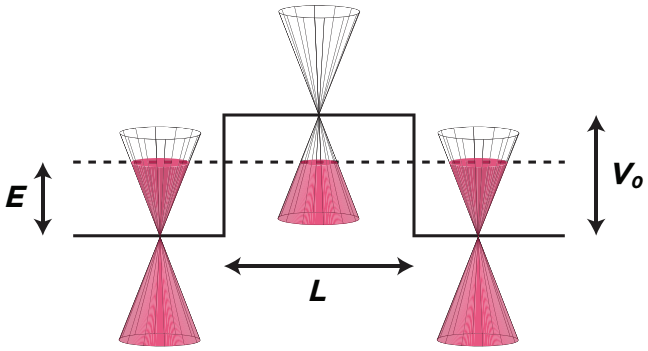

Figure 2.10: Klein tunnelling in graphene.

tion (2.15) is very similar to equation (2.8), except that the speed of light c, is used instead of the Fermi velocity $v_F \approx c/300$ [8].

The transmission probability for particles in graphene is derived to further emphasise the theory of Klein tunnelling. For simplicity, a perfectly rectangular potential barrier such as

$$V(x) = \begin{cases} V_0, & \text{if } 0 < x < L \\ 0, & \text{otherwise,} \end{cases} \tag{2.16}$$

is used, see figure 2.10. The Dirac-like Hamiltonian for graphene, sometimes referred to as the Weyl Hamiltonian[2], in equation (B.10), is used together with a factor for the potential barrier V_0. The incoming graphene particle is assumed to propagate with an angle γ_1 in respect to the x-axis. The expression for the transmission probability can be written as [8]

$$\begin{aligned} T &= 1 - |r|^2 \\ &= 1 - \left| 2ie^{i\gamma_1} \sin(c_1 L) \frac{\sin(\gamma_1) - c_2 \sin(\gamma_2)}{c_2 \left(e^{-ic_1 L} \cos(\gamma_1 + \gamma_2) + e^{ic_1 L} \cos(\gamma_1 - \gamma_2) \right) - 2i \sin(c_1 L)} \right|^2 \end{aligned} \tag{2.17}$$

[2]The Weyl Hamiltonian is described further in *Appendix B Weyl Hamiltonian for graphene*

where the variables are defined as

$$c_1 = \sqrt{\frac{(E - V_0)^2}{\hbar^2 {v_F}^2} - {k_y}^2}, \tag{2.18}$$

$$c_2 = \operatorname{sgn}(E)\operatorname{sgn}(E - V_0), \tag{2.19}$$

$$\gamma_2 = \arctan\left(\frac{k_y}{c_1}\right). \tag{2.20}$$

Equation (2.17) can be simplified for when $|V_0| \gg |E|$ as

$$T = \frac{\cos^2(\gamma_1)}{1 - \cos^2(c_1 L)\sin^2(\gamma_1)}. \tag{2.21}$$

The result in equation (2.21) show that perfect transmission always occurs when particles travel parallel to the x-axis, in other words when $\gamma_1 = 0$. The same applies for all values that satisfy $c_1 L = \pi n, n \in \mathbb{Z}$ [8]. In summary, for high enough barriers particles, who travel parallel to the x-axis, tunnel through unimpeded.

Throughout this section we have seen why Klein tunnelling is such an important trait to consider for graphene. The key fact to remember for graphene, is that both electrons and holes can be charge carriers in the channel at the same time. In regions where the particle energy is higher than the barrier energy, charge transport is assured by electrons, whereas when the particle energy is lower than the barrier energy, holes assure the charge transport role. Therefore in graphene devices, when one uses the term barrier, it does not indicate a region with total reflection or exponential dampening, but rather a region where charge transport is undertaken by holes instead of electrons [9].

2.7 Physical Parameter Values

When using graphene in electronic application it is important to know its exact physical parameter values. Table 2.1 contains a summary of important parameters for graphene. These values are used in this work, unless otherwise stated.

Parameter	Value	Unit	Reference
Carbon-carbon distance, a_{C-C}	1.42	Å	[6]
Mean free path, λ	0.3	μm	[20, 32]
Fermi velocity, v_F	10^6	m/s	[8–10]
Maximum current density	10^8	A/cm^2	[3, 20, 33]
Strength per density	48 000	kNm/kg	[3]

Table 2.1: Physical properties of graphene

Figure 2.11: Visual representation of the strength of graphene [35].

The extreme strength shown in graphene is because of the strong σ-bond between the carbon atoms. Professor James Hone of Columbia University expressed the strength of graphene in a very eloquent way [34]

> *Our research establishes graphene as the strongest material ever measured, some 200 times stronger than structural steel. It would take an elephant, balanced on a pencil, to break through a sheet of graphene the thickness of Saran Wrap.*

A visual representation of the expression is shown in figure 2.11.

Another well known and important trait for graphene is its mobility. The high mobility has often been seen as the main reason why researchers have had so high beliefs for material [3]. It has been shown that free standing graphene has the highest carrier mobility of all semiconductors [36, 37]. The carrier mobility, for free standing graphene, is limited almost only by the acoustic phonon scattering.

Yet, no parameter value for the mobility is shown in table 2.1. Graphene is usually placed on or between materials, which due to Coulomb scattering and optical surface phonons, decreases the mobility. Other factors such as the quality of graphene, temperature as well as applied electric field also effects the mobility in graphene [38]. To accurately calculate the carrier mobility, in a electronic device with graphene, these different effects have to be taken into consideration, hence why no static value can be added to table 2.1. The mobility is discussed further in *Section 5.2.6 Mobility*.

2.8 Applications

The chapter is concluded with this final section on the prospects and obstacles for electronic graphene applications.

There are many different areas where graphene is a prosperous material candidate for electronic applications. Experts talk about graphene having a big impact in technological fields such as wearable and flexible devices, photonic devices, nano-electromechanical systems (NEMS), solar cells, batteries, super dense data storages, bioelectronics as well as high-frequency devices. A closer look into patent applications shows that the dominant fields are synthesis and electronics which suggest that graphene is still at an early stage of development [3].

Graphene is process compatible with conventional processing of semiconductors, which puts the material in a favourable position [20]. Thanks to the process compatibility, it is possible to integrate graphene components in to silicon (Si)-based electronics with the possibility of gradually replacing Si [3]. The International Technology Roadmap for Semiconductors (ITRS) have stated that they consider graphene to be a possible candidate for post-Si electronics [39].

The first graphene integrated circuit, in which all components, including inductors and graphene field-effect transistors (GFETs), integrated on a wafer, was created in 2011 [1]. Positive results from the circuit showed that graphene devices with useful functionality and performance can be accomplished [3].

Using graphene as a channel material in transistors is an exciting idea because of the high mobility, current density and because particles in graphene show relativistic behaviour [3]. However, graphene gives a poor on-off current ratio due to its lack of energy band, which is why it is not suitable for logic circuits [16]. The missing band gap is often discussed as a big obstacle for graphene in electronic applications. A band gap can be opened, but it comes with the cost of decreased mobility. It has therefore been expressed that it would be better to use graphene in new applications rather than as a material to replace Si [1]. One example is negative differential resistance (NDR), a phenomena that is normally only seen in two-terminal devices [9].

In analogue and radio frequency (RF) circuits, a band gap is not as important. Instead, other figure of merit (FOM) such as the intrinsic gain A_v, maximum oscillation frequency f_{max} and cut-off frequency f_T play larger role, all of which are possible to achieve without a band gap [16]. The theory of intrinsic gain, maximum and cut-off frequency are described further in chapter *Chapter 3 Field-Effect Transistor*.

For possible applications, the problems with manufacturing has to be overcome. The cost of manufacturing good quality graphene is today too high for

commercial use. Different techniques are developed and used to create graphene; micro-mechanical cleavage, chemical vapour deposition (CVD), growth on alternative substrates as silicon carbide (SiC) and hexagonal boron nitride (h-BN) are among some of the most common techniques [3]. Micro-mechanical cleavage was the technique originally used by Andre Geim and Konstantin Novoselov [40]. The technique was for a long time the best to get large single crystalline structures. It is still often used in fundamental research because of its low cost and simplicity. In essence, the only tools needed are a pencil and some tape. CVD is a useful processing technique since it is used commercially for many other materials, however the method still has to improve to consistently create large single crystalline graphene sheets. Growth on alternative substrates have several benefits such as speed, better lattice match and higher control over the thickness to ensure that only one monolayer is deposited. But even though both SiC and h-BN give better results quicker, the cost is still too high compared to conventionally used Si substrates. In 2011, the cost of SiC was about 25-30 times more expensive than Si [3].

Chapter 3

Field-Effect Transistor

A field-effect transistor (FET) is an electronic device with at least three terminals: source, drain and gate. A channel, where the current can flow, is in between the source and drain. An insulator is placed in between the channel and the gate terminal. Figure 3.1 shows this conventional layout. In most conventional FETs silicon (Si) is used as a channel material [3].

As its name suggests, FETs relies on an electric field. When a potential is applied to the gate, an electric field is created. The electric field repels or attracts electrons in the channel thereby altering the number of free charge carriers (electrons or holes) available for conduction, hence changing the channel conductivity [41]. The transistor is in its on-state when the free carrier density in the channel is high, on the contrary when the free carrier density is low the transistor is said to be in its off-state. Conventional FETs are unipolar transistors meaning that the majority charge carriers in the channel are electrons or holes [20].

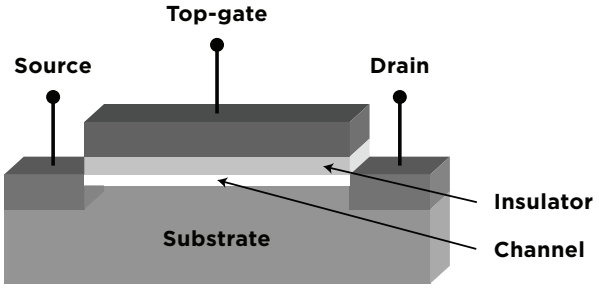

Figure 3.1: Layout of typical FET.

3.1 Analogue Amplifier

FETs can be used in logic or analogue and radio frequency (RF) applications. In the latter case, the FETs are commonly used as analogue amplifiers. A typical set-up is shown in figure 3.2. A potential V_{gs} applied between gate and source, controls the current I_{ds} flowing between drain and source. The current I_{ds} flows through the resistor R_L, causing a voltage drop and therefore the output potential V_{out} is altered. The difference between the output V_{out} and input voltage $V_{in} = V_{gs}$ gives the important figure of merit (FOM) called intrinsic voltage gain,

$$A_v = \frac{V_{out}}{V_{in}} = \frac{V_{out}}{V_{gs}}. \tag{3.1}$$

From the definition, it can be seen that the intrinsic voltage gain depends on both the transconductance,

$$g_m = \frac{dI_{ds}}{dV_{gs}}, \tag{3.2}$$

and the load resistance, R_L. To improve the value of A_v, large currents must be achieved. This can be done by enhancing the carrier concentration and velocity. There are different methods that can be used for enhancement, some common methods include channel doping, channel material choice as well as size reduction of channel and gate insulator [20].

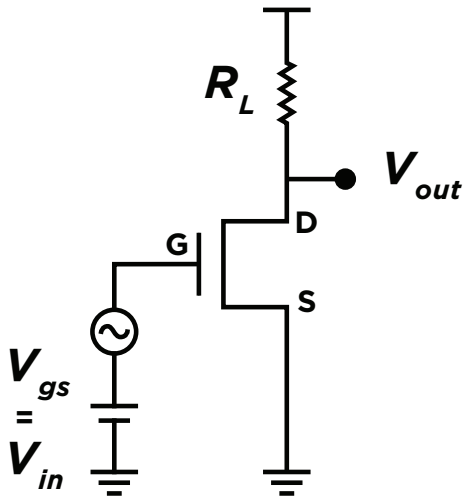

Figure 3.2: Schematic of an analogue amplifier using FET.

Voltage gain $A_v > 1$ is required in general-purpose electronic circuits, such as analogue voltage amplifiers and digital logic gates. [3]

Two other important FOM is the cut-off frequency f_T and the maximum oscillation frequency f_{max}. The cut-off frequency is defined as the frequency at which the energy flowing through the system is no longer attenuated. This occurs when intrinsic current gain decreases to unity, so that the current gain is 0 dB . The maximum oscillation frequency on the other hand, is defined as the frequency at which the power gain is 0 dB [7].

Chapter 4

Graphene Field-Effect Transistor

In graphene field-effect transistors (GFETs), the channel material is graphene. The first GFET was reported in 2004, this was a back-gated device that showed that it was possible to use graphene as a channel material. However, the transistor had intrinsic voltage smaller than unity $A_v < 1$, and it suffered from large parasitic capacitances and therefore could not be integrated with other components [3]. The first graphene metal-oxide-semiconductor field-effect transistor (MOSFET) was reported in 2007. The results showed that the current could be controlled with the applied gate voltage and the envisaged capability of GFETs was confirmed [13]. After that a number of transistors, that use graphene as a channel material, have been successfully fabricated [3]. In 2010, a report showed a successful fabrication of a GFET with $A_v > 1$ [42]. Year 2012, a group of researchers fabricated a GFET with 67 nanometer (nm) gate length and the impressive cut-off frequency $f_T = 427$ GHz [43]. The fast development of GFETs is a good indicator for the potential of the device.

In this chapter we will discuss the theory behind GFETs. The chapter begins with *Section 4.1 Basic Principles* where the basic principles are explained along with some notations. *Section 4.2 Carrier Density Inside the Channel* further explores the carrier density as well as the channel potential V_{ch}, for different biasing conditions. The chapter is concluded with *Section 4.3 Negative Differential Resistance*, where the theoretical explanation as well as needed biasing conditions for negative differential resistance (NDR) are discussed.

4.1 Basic Principles

A very basic GFET-layout is used in this work. Starting with a wafer, an oxide layer is deposited. The oxide both acts as a back-gate oxide as well as a material onto which graphene can be grown more easily. The combination of silicon (Si) wafer and silicon dioxide (SiO_2) is commonly mentioned in literature [3, 44, 45]. On the oxide the graphene layer is grown, and subsequently the source and drain terminals as well as the gate-oxide and the gate terminal. The back terminal is placed at the bottom of the sample. See figure 4.1 for a visual representation. It is conventional to ground the source and consider it the reference potential in the device [16]. For simplicity, only the part under the gate terminal is considered in GFET simulations, this region is called the intrinsic device [14].

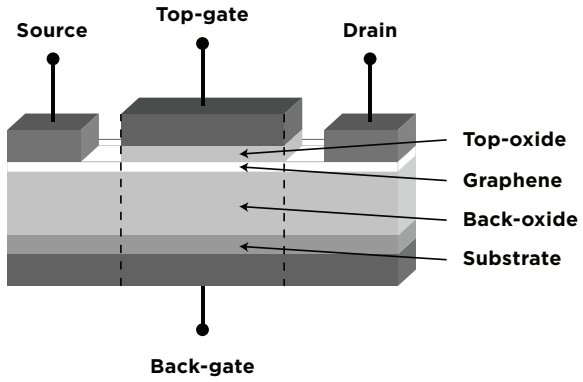

Figure 4.1: Layout of typical GFET.

The carrier concentration in the channel is modulated by the applied gate-to-source voltage V_{gs}. In figure 4.1, as in many GFETs, two gates are used to modulate the potential: top-gate V_{gs-top} and back-gate $V_{gs-back}$ [16]. The applied voltages creates a field-effect in the channel which repels or attracts electrons or holes. To achieve a high effect for the applied potentials V_{gs-top} and $V_{gs-back}$, it is important to use thin and high-K (dielectric constant) oxides between the gates and the channel [3].

The Dirac voltage V_{dirac}, is a parameter commonly used in analysis, modelling and discussions of GFETs. We have earlier in this report defined it as the gate potential when the Fermi-level E_f, passes through the Dirac point E_d, see *Section 2.5 Charge Density*. This still holds true for GFETs, if there is no charge difference between source and drain $V_{ds} = 0$. For that particular case one could think of V_{dirac} as the gate potential where the majority charge concentration in the channel changes sign [6, 46]. However, for the more general case the Dirac

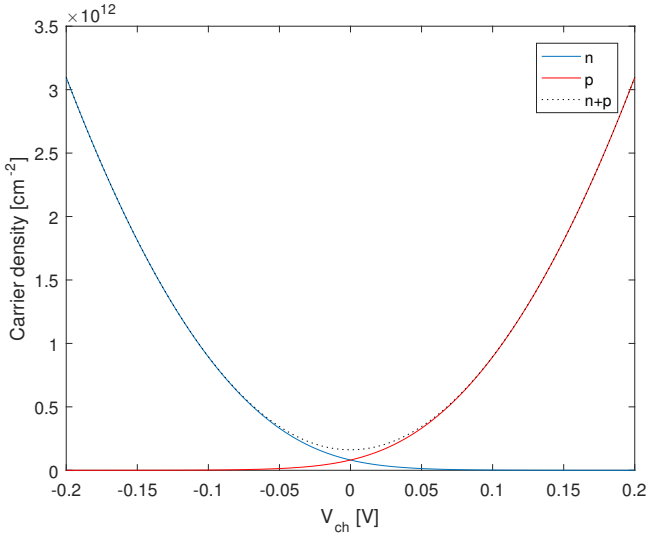

Figure 4.2: Carrier densities for electrons n and holes p, versus channel potential V_{ch}.

potential is often defined as the gate voltage at minimum current [20]. As will become evident, the Dirac voltage changes with applied drain-to-source voltage, which is why in this report we will refer to $V_{dirac-0}$ as the Dirac voltage when $V_{ds} = 0$. This way $V_{dirac-0}$ stays constant, even for changed biasing conditions.

The Dirac voltage should not be confused with the flat-band voltage, V_{fb}, which is defined as the voltage needed for no electric field to exist over the oxide [16, 20].

4.2 Carrier Density Inside the Channel

It is crucial to understand how applied potential effects the characteristics and potential inside the GFET channel.

4.2.1 Channel Potential

The potentials at the source, drain and gate terminals effects both the level of the Dirac point E_d, as well as the Fermi level E_f. The difference between E_f and E_d is of great importance as it determines the type of charge as well as the charge density in the channel. The relationship

$$E_f - E_d = -qV_{ch}, \tag{4.1}$$

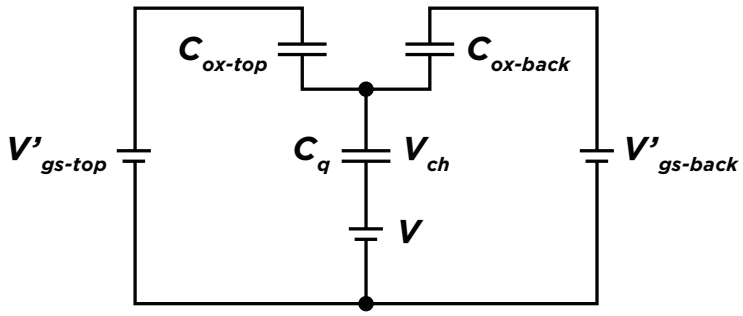

Figure 4.3: Equivalent circuit of GFET electrostatics used to calculate the channel potential V_{ch}.

is commonly used, where V_{ch} is known as the channel potential. If $V_{ch} < 0$, then E_f is above E_d, on the contrary if $V_{ch} > 0$, then E_f is below E_d [15]. V_{ch} is discussed and used in many GFET simulations and in modelling, we will therefore often refer to it instead of E_d and E_f [14–16, 47, 48]. V_{ch} can be substituted into equations (2.10) and (2.11), hence giving

$$n = \frac{2(kT)^2}{\pi(\hbar v_F)^2}\mathfrak{F}_1\left(-\frac{qV_{ch}}{kT}\right), \tag{4.2}$$

$$p = \frac{2(kT)^2}{\pi(\hbar v_F)^2}\mathfrak{F}_1\left(\frac{qV_{ch}}{kT}\right). \tag{4.3}$$

Figure 4.2 shows a plot of equations (4.2) and (4.3). In the figure, the effect of the channel potential on the carrier density is clear; for $V_{ch} < 0$, the carrier density of electrons will be the highest, while for $V_{ch} > 0$ the carrier density for holes will be the highest.

To calculate V_{ch} in GFETs, an equivalent capacitive circuit of the GFET gate electrostatics can be used, see figure 4.3. Both top- and back-gate potentials are regulated as

$$V_{gs-top}{}' = V_{gs-top} - V_{dirac-0-top}, \tag{4.4}$$

$$V_{gs-back}{}' = V_{gs-back} - V_{dirac-0-back}. \tag{4.5}$$

V_{gs-top} and $V_{gs-back}$ are the applied top- and back-gate voltages while $V_{dirac-0-top}$ and $V_{dirac-0-back}$ are the Dirac voltages when $V_{ds} = 0$ as well as when the respective gate voltage is zero. $V_{gs-back} = 0$ for $V_{dirac-0-top}$ and $V_{gs-top} = 0$ for $V_{dirac-0-back}$. [15]. The gate-oxide capacitance for respective top- and back-gate

are calculated as

$$C_{ox-top} = \frac{\varepsilon_{ox-top}}{t_{ox-top}}, \tag{4.6}$$

$$C_{ox-back} = \frac{\varepsilon_{ox-back}}{t_{ox-back}}, \tag{4.7}$$

where t is the oxide thickness and ε is the oxide permittivity [45]. The exact expression for the quantum capacitance C_q is [14, 49]

$$C_q = \frac{2q^2kT}{\pi(\hbar v_F)^2} \ln\left(2\left(1+\cosh\left(\frac{qV_{ch}}{kT}\right)\right)\right). \tag{4.8}$$

V in figure 4.3 is the voltage drop between the channel and ground. V gets a relatively simple expression when source is grounded; at the source end the voltage drop is zero $V(x=0)=0$, while at the drain end the voltage drop it is equal to the drain-to-source voltage $V(x=L)=V_{ds}$ [16].

The expression

$$V_{ch} = -\frac{(V_{gs-top}{}' - V)\cdot C_{ox-top} + (V_{gs-back}{}' - V)\cdot C_{ox-back}}{C_{ox-top} + C_{ox-back} + \alpha(V_{ch})C_q(V_{ch})}, \tag{4.9}$$

can be derived from figure 4.3 [15, 45]. The simplified expression

$$V_{ch} = -\frac{(V_{gs-top}{}' - V)\cdot C_{ox-top}}{C_{ox-top} + \alpha(V_{ch})C_q(V_{ch})}, \tag{4.10}$$

should be used if the device does not have a back-gate terminal [48].

$$\alpha = \frac{kT}{qV_{ch}} \cdot \frac{\mathfrak{F}_1\left(\frac{qV_{ch}}{kT}\right) - \mathfrak{F}_1\left(-\frac{qV_{ch}}{kT}\right)}{\ln\left(2\left(1+\cosh\left(\frac{qV_{ch}}{kT}\right)\right)\right)}, \tag{4.11}$$

is the capacitance weighting factor [15]. It is possible to calculate the value of V_{ch} in both equations (4.9) and (4.10), if the values of V and V_{gs} are known.

4.2.2 Biasing Configurations

Different biasing configurations are studied in this section, to get a better understanding of the carrier density inside the channel of GFETs. No back-gate is used for the sake of simplicity, and the top-gate is therefore denoted as V_{gs}. The source is grounded in all configurations. Visual images are used to give a clearer understanding of how the channel looks, but note that the images are representative rather than mathematically correct. However, as shown in the images, the voltage drop in the channel should always be the highest when the Fermi energy passes through the Dirac point, as the resistivity there is the

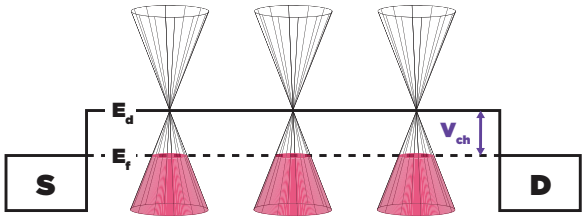

(a) Scenario A.1.

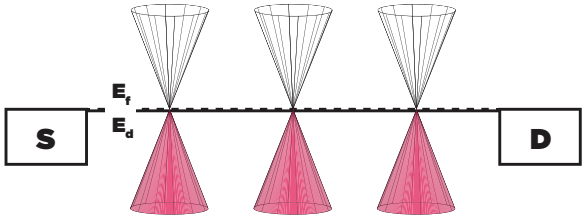

(b) Scenario A.2.

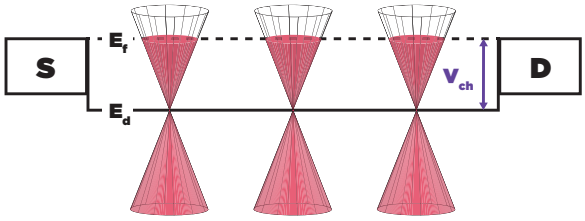

(c) Scenario A.3.

Figure 4.4: First instance of scenarios.

highest [45, 50].

In the first instance, scenarios A.1–A.3, it is assumed that there is no potential difference between source and drain, $V_{ds} \approx 0$.

Scenario A.1: $V_{gs} < V_{dirac}$. In this scenario E_f is below E_d, $V_{ch} > 0$. From figure 4.2, this means that there will be a high concentration of holes. For decreased values of V_{gs}, E_f and E_d move further away from each other, which increases the hole concentration and thereby the conductivity in the channel. But, when V_{gs} is increased, E_f and E_d move closer together, thereby decreasing V_{ch}.

Scenario A.2: $V_{gs} = V_{dirac}$. With this applied potential, E_f goes through E_d, $V_{ch} = 0$. This means that the minimum charge density for electrons and holes is reached, see figure 4.2. The conductivity in the channel is very low.

Scenario A.3: $V_{gs} > V_{dirac}$. In this scenario, E_f is above E_d, $V_{ch} < 0$. As

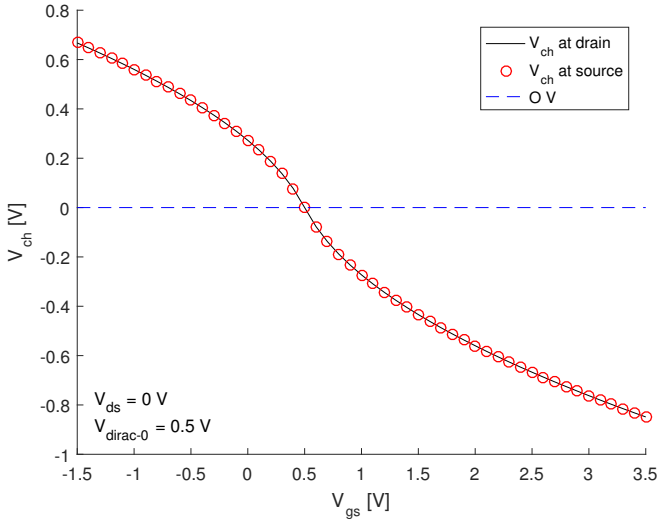

Figure 4.5: Channel potential V_{ch} for when the drain-to-source voltage $V_{ds} \approx 0$ V and the Dirac voltage $V_{dirac-0} = 0.5$ V, scenario A.1-A.3.

can be seen in figure 4.2, this means that the electron density is high. As V_{gs} is increased, E_f and E_d move further apart, decreasing V_{ch} and therefore increasing the electron concentration, hence again increasing the conductivity in the channel [16].

Equation (4.10) is used in MATLAB [18] to calculate V_{ch} in scenarios A.1–A.3, the result is displayed in figure 4.5. V_{ch} is calculated at source and drain, since V is only known at these points. The results are in good agreement with the theory. V_{ch} has the same value at both source and drain, and as expected V_{ch} changes sign at $V_{gs} = V_{dirac}$. The correlating charge densities are also calculated at source and drain, see figure 4.6. In the figure it is somewhat difficult to see all curve values since they overlap. Nevertheless, we can see that the results agree with the theory and that same pattern is followed; first high charge density for holes, which becomes smaller as V_{gs} increases towards V_{dirac}. When $V_{gs} > V_{dirac}$ electrons dominate the channel, with increasing density for larger values of V_{gs}.

Moving on, in the second instance of scenarios, it is assumed that $V_{ds} \gg 0$ creating a clear potential difference between source and drain. This means that charges can flow in the channel.

Scenario B.1: $V_{gs} < V_{dirac-0}$. In this scenario, E_f is below E_d everywhere in the channel, $V_{ch} > 0$. The hole density is high and holes travel from drain to source generating a current in the same direction. Holes are said to be

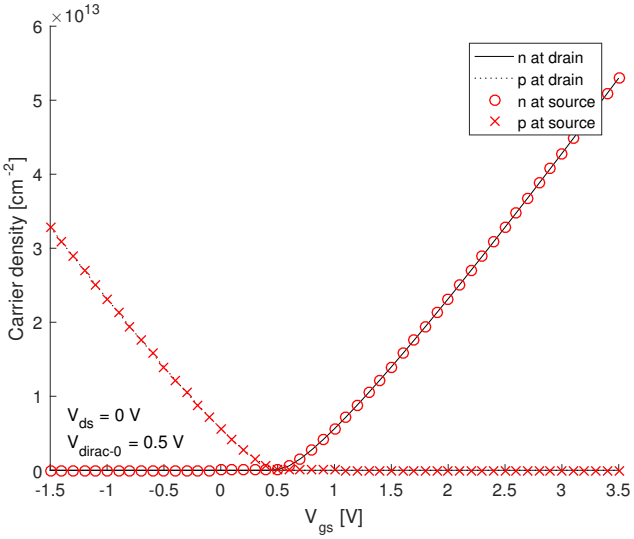

Figure 4.6: Carrier density when the drain-to-source voltage $V_{ds} \approx 0$ V and the Dirac voltage $V_{dirac-0} = 0.5$ V, scenario A.1-A.3.

the majority charge carriers. As V_{gs} increases the difference between E_d and E_f decreases, which means the hole density will decrease, which decreases the channel conductivity and thereby the current.

Scenario B.2: $V_{gs} = V_{dirac-0}$. In this scenario, E_f coincides with E_d at the source end, $V_{ch} = 0$. This occurrence is often referred to as the Dirac cone being introduced into the channel, see figure 4.7b. Of course, one should note that the Dirac cones are not moving into the channel, it is merely an expression. It would have been more correct to say that at this occurrence, there is a point in the channel where E_f and E_d coincide. E_f is below E_d in the rest of the channel, $V_{ch} > 0$. Holes are still majority charge carriers for this scenario, but the channel conductivity is lower compared to scenario B.1 [16]. The local channel resistivity is inversely proportional to the local carrier density, which means that most of the voltage drop occurs at the source side where the local carrier density is the lowest [50].

Scenario B.3: $V_{dirac-0} < V_{gs} < V_{dirac-0} + V_{ds}$. Increasing the potential further creates this interesting scenario. E_f is above E_d, $V_{ch} < 0$, in part of the channel, while E_f is below E_d, $V_{ch} > 0$, in the other part of the channel. At the side closest to source, where $V_{ch} < 0$, there is a high density of free electrons. The potential difference, V_{ds}, will push the electrons from source to drain, contributing to the current in the opposite direction. Simultaneously, on the drain side, where $V_{ch} > 0$, holes will have a higher density and the potential differ-

ence will push the holes from drain to source, contributing to the current in the same direction. Increased gate voltage will decrease the part where $V_{ch} > 0$, hence decreasing the hole density, this it is often described as the Dirac cone moving further into the channel. When the Dirac cone reaches the middle of the channel both carrier concentrations are equal. However, the minimum current will probably not occur exactly at this point, since the mobility of holes and electrons often differ.

Scenario B.4: $V_{gs} = V_{dirac-0} + V_{ds}$. E_f and E_d coincide, $V_{ch} = 0$, at the drain side and in the rest of the channel $V_{ch} < 0$. One could say that at this point the Dirac cone have moved all the way through the channel from the source to the drain side.

Scenario B.5: $V_{gs} > V_{dirac-0} + V_{ds}$. As the voltage continues to increase E_f and E_d move away from each other everywhere in the channel, $V_{ch} < 0$. The electron density and the conductivity thereby continue to increase [16].

Calculations are again made with MATLAB [18] for scenarios B.1–B.5. The results are displayed in figures 4.8 and 4.9. Figure 4.8 shows that the source side is $V_{ch} = 0$ when $V_{gs} = V_{dirac-0}$, while at drain end is $V_{ch} = 0$ first at $V_{gs} = V_{dirac-0} + V_{ds}$. As expected, that means that for certain values V_{ch} have different signs throughout the channel, meaning that both electrons and holes will be charge carriers and thereby contribute to the current. This can also be seen clearly in figure 4.9 where the type of majority charge carriers differs from source and drain when $V_{dirac-0} < V_{gs} < V_{dirac-0} + V_{ds}$.

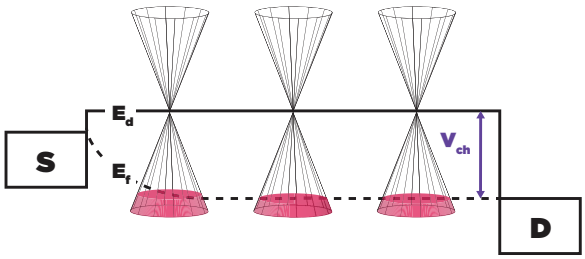

(a) Scenario B.1.

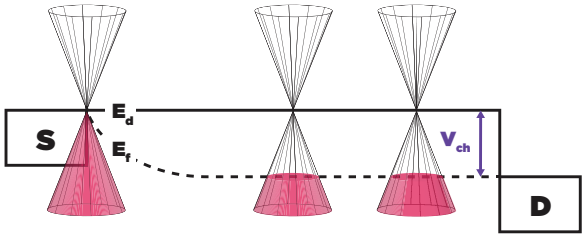

(b) Scenario B.2.

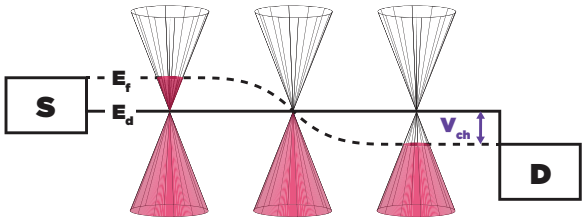

(c) Scenario B.3.

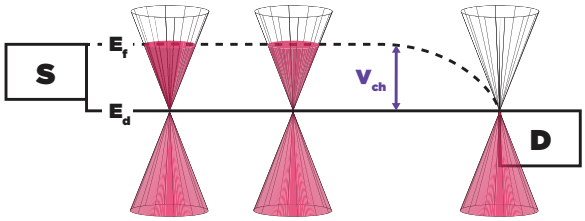

(d) Scenario B.4.

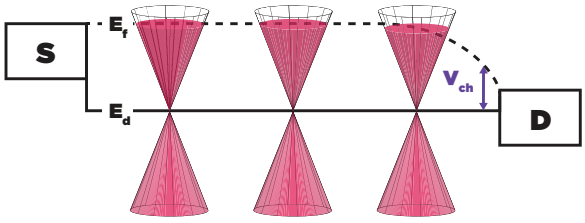

(e) Scenario B.5.

Figure 4.7: Second instance of scenarios.

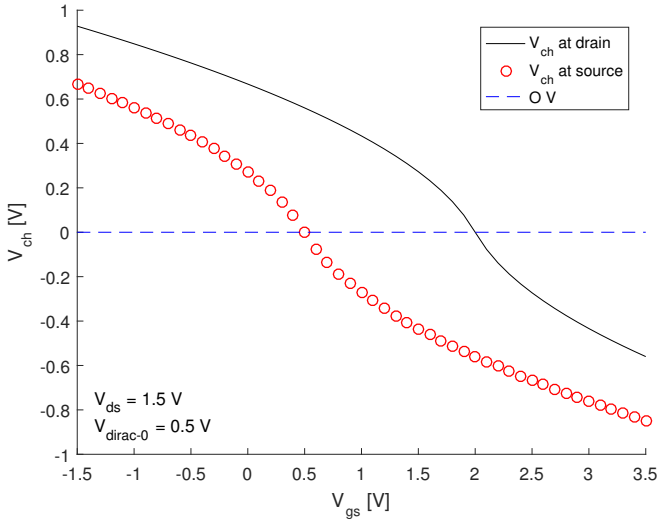

Figure 4.8: Channel potential V_{ch} when the drain-to-source voltage $V_{ds} \approx 1.5$ V and the Dirac voltage $V_{dirac-0} = 0.5$ V, scenarios B.1–B.5.

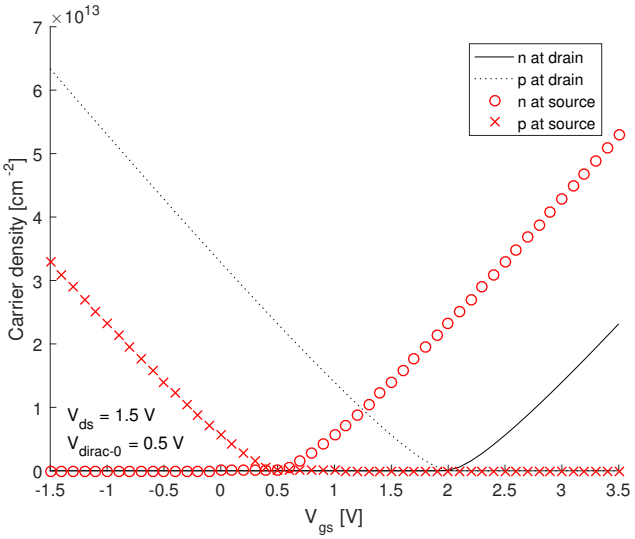

Figure 4.9: Carrier density when the drain-to-source voltage $V_{ds} \approx 1.5$ V and the Dirac voltage $V_{dirac-0} = 0.5$ V, scenarios B.1–B.5.

For these first two instances of scenarios, A and B, V_{ds} has been constant while the value of V_{gs} has increased. Let us now continue by looking at a third and last instance of scenarios where V_{gs} is static while V_{ds} changes, here

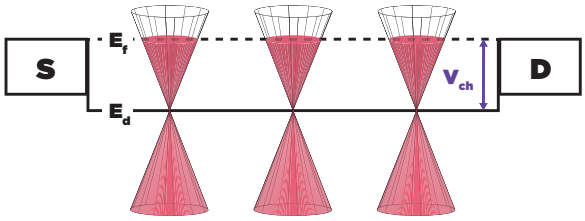

(a) Scenario C.1.

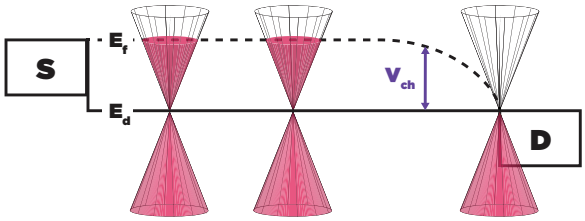

(b) Scenario C.2.

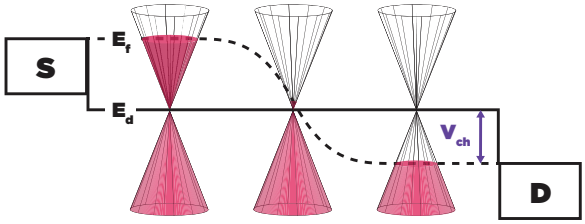

(c) Scenario C.3.

Figure 4.10: Last instance of scenarios.

$V_{gs} \gg V_{dirac-0}$.

Scenario C.1: $V_{ds} = 0$. In the first scenario, no potential is applied between source and drain. E_f is above E_d, with $V_{ch} < 0$ having the same value everywhere in the channel. Even though there is a large electron density everywhere in the channel, the total current, I_{ds}, will be very small due to the lack of potential difference between source and drain. If V_{ds} is decreased, the gap between E_f and E_d gets wider, hence increasing the carrier density of electrons, but it would also creating a potential difference, that would generate a current.

Scenario C.2: $V_{ds} = V_{gs} - V_{dirac-0}$. At this point, the Dirac cone is introduced into the channel on the drain side, $V_{ch} = 0$. The difference between E_f and E_d at the source side does not change, hence why V_{ch} at the source end remains the same. The potential difference in the channel makes electrons go from source to drain, generating a current in the opposite direction.

Scenario C.3: $V_{ds} > V_{gs} - V_{dirac}$. E_f is below the E_d, $V_{ch} > 0$, close to the drain side. As V_{ds} continues to increase, the Dirac cone moves throughout the channel. However, since V_{ch} remains constant the source end, the Dirac cone cannot move all the way. The channel will have both negative and positive V_{ch}, meaning that both electrons and holes will contribute to the current [16].

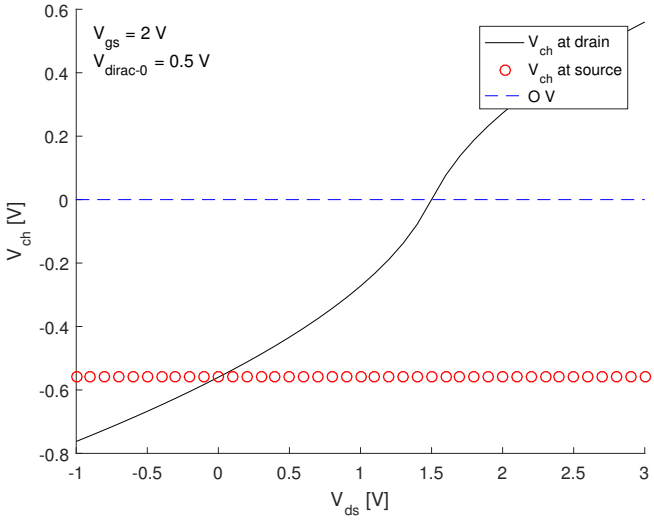

Figure 4.11: Channel potential V_{ch} when the gate-to-source voltage $V_{gs} = 2.0$ V and the Dirac voltage $V_{dirac-0} = 0.5$ V, scenarios C.1–C.3.

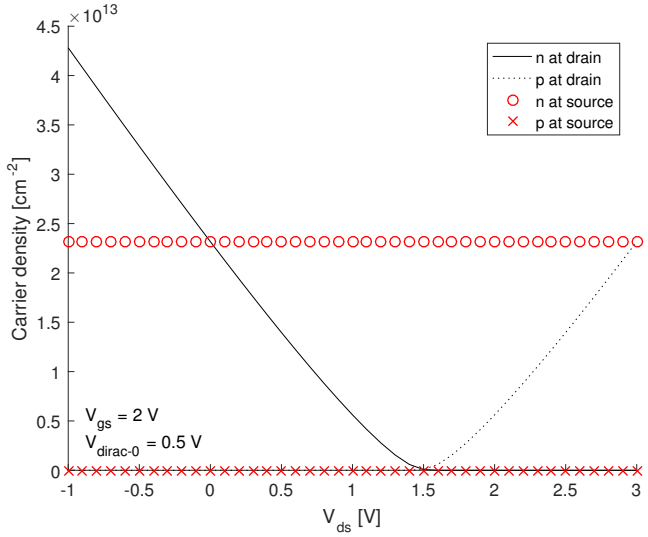

Figure 4.12: Carrier density when the gate-to-source voltage $V_{gs} = 2.0$ V and the Dirac voltage $V_{dirac-0} = 0.5$ V, scenarios C.1–C.3.

Final calculations using MATLAB [18] are displayed in figures 4.11 and 4.12. In figure 4.11, the theory of V_{ch} remaining constant at the source end is confirmed. It is also shown that the potential V_{ch} at the drain end, change sign at $V_{gs} = V_{gs} - V_{dirac-0}$, just like anticipated. In figure 4.12, it can be seen that both electrons and holes will contribute to the current for $V_{ds} > V_{gs} - V_{dirac-0}$.

In summary, the most important thing that we can note from this is that in some scenarios, both electrons and hole contribute to the total current. In regions where $V_{ch} < 0$, charge transport will be assured by electrons, and on the contrary where $V_{ch} > 0$, holes assume the charge transport role.

When discussing general field-effect transistors (FETs), it is accustomed to express the channel as either n-type, when electrons are charge carriers, or p-type, when the charge carriers are holes. That the channel can be adjusted, to be both n- and p-type, is referred to the transistor as having ambipolar characteristics. This is an unusual trait of FETs, since most conventional transistors are either n- or p-type, not both [8, 9].

4.3 Negative Differential Resistance

An interesting phenomena, that in GFETs is associated with the ambipolar transport, is the negative differential resistance (NDR). The term negative resistance refers to when an increased voltage across a device's terminals results

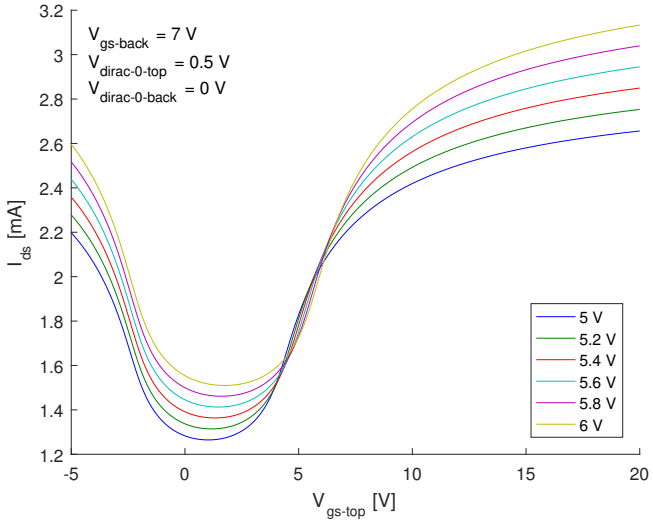

Figure 4.13: Drain-to-source current I_{ds}, versus gate-to-source potential V_{gs}. $V_{ds} = 5 - 6$ V, $V_{gs-back} = 7$ V, $V_{dirac-0-top} = 0.5$ V and $V_{dirac-0-back} = 0$ V.

in a decrease in the electric current. Mathematically NDR can be described as

$$\frac{\Delta v}{\Delta i} < 0, \tag{4.12}$$

while

$$\frac{dI_{ds}}{dV_{ds}} < 0. \tag{4.13}$$

is used more specifically for GFETs [9]. Theoretical and experimental results show that NDR occurs in GFETs with all sorts of graphene quality, oxides and gate lengths [9, 38, 50]. It is a general feature of graphene that occurs under certain biasing conditions [50]. Other devices where NDR can be observed are resonant tunnel diodes, single-electron-transistors and Esaki diodes. These devices have a high peak-to-valley current ratio but they suffer due to low peak current densities. Because of the high current carrying capabilities of GFETs, the devices do not suffer from low peak current densities [38], which is one of the main advantages with using GFETs for NDR. Another advantage, is that it is a three-terminal device, where the gate controls the current flow, which means that the NDR behaviour can be switched on and off.

4.3.1 Theoretical Explanation

In 2012, a group of researchers proposed that the NDR phenomena, in GFETs, occurs as a result of the ambipolar transport [50]. However in 2015, Sharma et

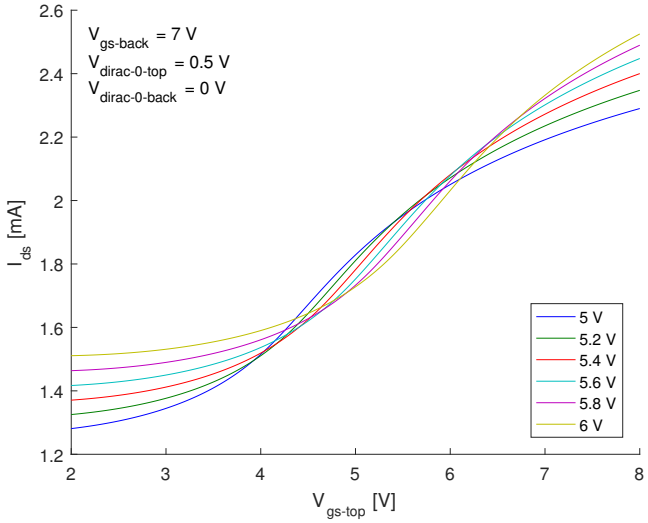

Figure 4.14: Enlargment of figure 4.13 showing the drain-to-source current I_{ds}, versus gate-to-source potential V_{gs}. $V_{ds} = 5 - 6$ V, $V_{gs-back} = 7$ V, $V_{dirac-0-top} = 0.5$ V and $V_{dirac-0-back} = 0$ V.

al. showed that the ambipolar transport can only be part of the reason. The group proposed that NDR occurs due to the competition between the carrier drift velocity and carrier density [38].

A double-gated GFET model is simulated in Advanced Design System (ADS) [17] and displayed using MATLAB [18] in figure 4.13. The simulation model is described further in *Section 5.2.10 Simulation Model 3*. Figure 4.13 shows I_{ds} versus V_{gs-top} for six different values of V_{ds}. As can be seen, the point of minimum current moves to the right for increased potential which leads to an overlap in the curves around 5 V. The area is enlarged in figure 4.13, between 5 and 6 V it is clear that the simulations with less applied potential V_{ds}, produce larger currents. This means, that for these bias values NDR behaviour should be visible. A new simulation is therefore made with the potential value V_{gs-top} chosen somewhere in the region where the curves overlap. The simulation results are shown in figure 4.15, where NDR is clearly visible.

The value of dI_{ds}/dV_{ds} is shown in figure 4.16, to more easily observe where the negative differential starts and ends. Extracted from the figure, the NDR occurs around $V_{ds} \approx 5-6$ V. To understand the behaviour, the channel potential V_{ch} as well as the carrier densities n and p, are calculated using equations (4.2), (4.3) and (4.9), as in previous scenarios. Figures 4.17 and 4.18 show the result of the calculations. I_{ds} increases linearly for low values of V_{ds}, however from figure 4.18, it can be seen that the electron carrier density decreases with in-

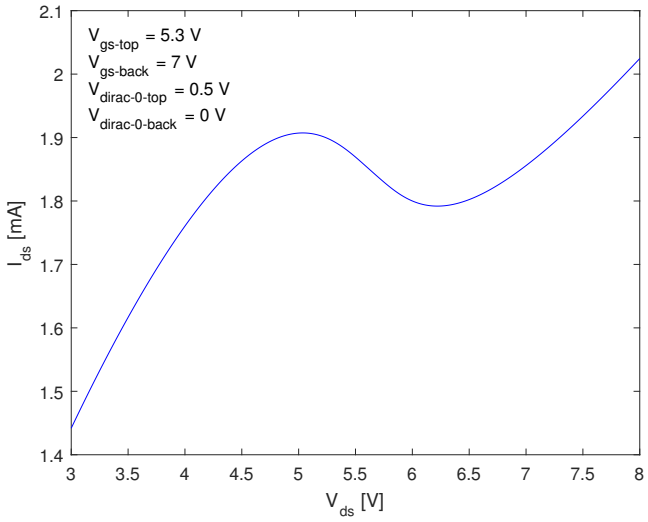

Figure 4.15: Drain-to-source current I_{ds}, versus drain-to-source potential V_{ds}. $V_{gs} = 5.3\ V$, $V_{gs-back} = 7\ V$, $V_{dirac-0-top} = 0.5\ V$ and $V_{dirac-0-back} = 0\ V$.

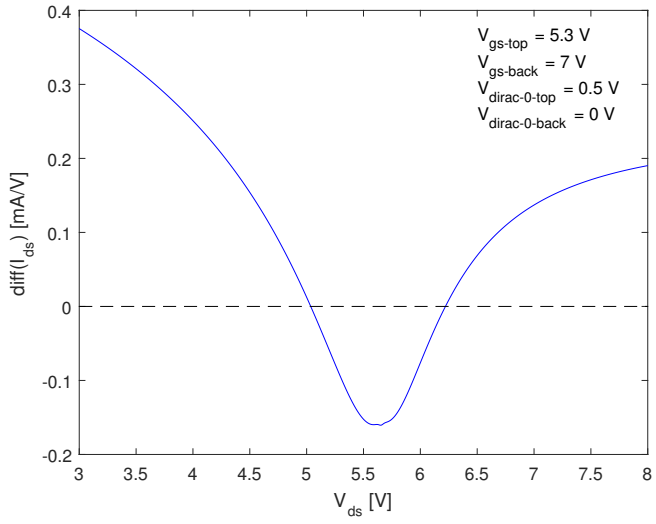

Figure 4.16: Differential dI_{ds}/dV_{gs}, versus drain-to-source potential V_{ds}. $V_{gs} = 5.3\ V$, $V_{gs-back} = 7\ V$, $V_{dirac-0-top} = 0.5\ V$ and $V_{dirac-0-back} = 0\ V$. NDR behaviour is visible around $V_{ds} \approx 5 - 6\ V$.

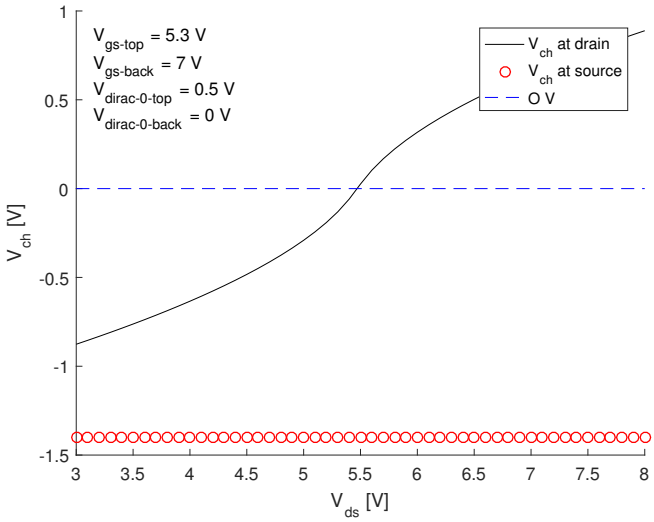

Figure 4.17: Channel potential V_{ch}, versus applied drain-to-source potential V_{ds}. $V_{gs} = 5.3\ V$, $V_{gs-back} = 7\ V$, $V_{dirac-0-top} = 0.5\ V$ and $V_{dirac-0-back} = 0\ V$.

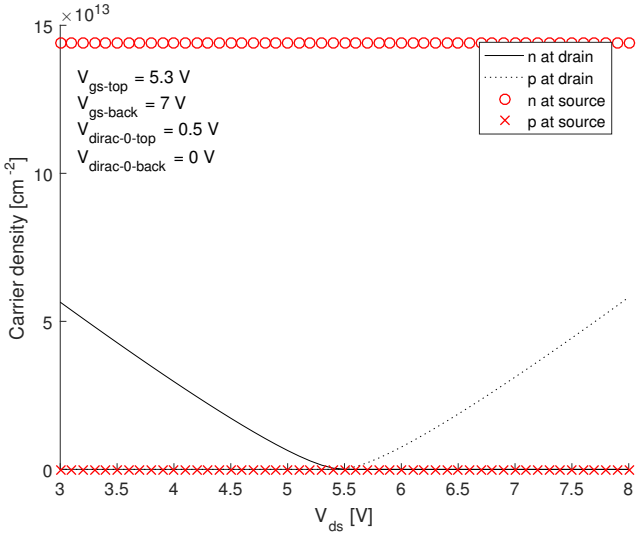

Figure 4.18: Charge densities n and p, versus channel potential V_{ch}. $V_{gs} = 5.3\ V$, $V_{gs-back} = 7\ V$, $V_{dirac-0-top} = 0.5\ V$ and $V_{dirac-0-back} = 0\ V$.

creased V_{ds}. The current continues to grow because a greater potential leads to an increased drift velocity. The drift velocity continues to increase until it reaches the velocity saturation, which is inversely proportional to the square root of the total carrier density. This means that the velocity saturation is high for low carrier densities, while the velocity saturates at lower values for high carrier densities [45].

If NDR is wanted in a GFET, it is important to know about the physics behind the phenomena as it will help when choosing biasing conditions. For NDR to be visible an increase in the potential V_{ds} needs to lead to a decrease in carrier density. However, the total carrier density should be large enough to cause velocity saturation [45], otherwise no NDR will be visible. This often means applying large gate potentials, which has been done in this simulation example.

Chapter 5

Modelling Graphene Field-Effect Transistor

In this chapter, different simulation models for graphene field-effect transistors (GFETs) are investigated further. All models must be compatible with the hardware description language Verilog-A. This means that we are restricted to the models that we can solve analytically, since the program cannot solve equations numerically. However, equations are solved numerically in MATLAB [18], to compare and validate calculations as well as approximations before implementation. The full models are run using the simulation program Advanced Design System (ADS) [17].

The general current expression for GFETs can be written as

$$I_{ds} = -WQ(x)v_{drift}(x), \tag{5.1}$$

where W is the width of the channel, Q is the charge carrier density and v_{drift} is the drift velocity of the carriers [14, 16, 45, 51]. The assumptions, calculations and approximations made to 5.1 will determine the accuracy of the model.

This chapter contains four different simulation models, all of which have been implemented in Verilog-A and run with ADS [17]. All models have been explained and most calculations are shown explicitly. The chapter begins with *Section 5.1 Ballistic Transport* that clarifies how transistor length effects what model that can be used. *Section 5.2 Drift-Diffusion Model* compares different parameter approximations for the drift-diffusion (DD) model, all calculations and graphs are displayed using MATLAB [18]. Finally, *Section 5.3 Virtual Source Model* gives a short introduction into the virtual source (VS) model.

5.1 Ballistic Transport

The basic concept of local equilibrium have been discussed in *Section 2.4 Local Equilibrium*. The assumption of local equilibrium in GFETs is based on the fact that electrons scatter and collide inside the channel. The average length each electron travels before a scattering event is called the mean free path λ [25]. When the channel length becomes smaller, going towards λ, the carriers start travelling without experiencing any collisions or scatterings that impede their motion. This type of transport is called ballistic transport. When no scattering or collisions occur, the assumption of local equilibrium is no longer valid. Therefore no (quasi-)Fermi levels can be defined, which is one of the reasons why modelling of ballistic semiconductors is more complicated [52]. The mean free path for graphene, see table 2.1, is relatively long which means that ballistic transport cannot be ignored even for transistors that normally are seen as long channel devices. Additionally, ballistic behaviour for GFETs has been detected for device lengths longer than 10 μm [3].

5.1.1 Quasi-Ballistic Transport

In literature, the common way to denote quasi-ballistic transport, is any device in which ballisticity can be detected to such degree that it cannot be neglected, irrespectively of the channel length [25, 53]. In quasi-ballistic devices, high energy carriers travel ballistically while other particles travel diffusively. This means that a model for quasi-ballistic transport has to consider both collision-free and collision-dominated transport [53].

One interesting point in quasi-ballistic transport models is that quasi Fermi levels cannot be determined. This makes the carrier mobility a questionable concept from a theoretical standpoint. Nevertheless, the mobility can still be measured practically even in the smallest devices [54].

5.2 Drift-Diffusion Model

The drift-diffusion (DD) model is commonly used in literature as well as scientific reports. The model is made under the assumption of local equilibrium. Local equilibrium enables calculations of local quasi-Fermi levels, from which the carrier distribution can be calculated using Fermi-Dirac statistics [25]. However, because local equilibrium must be established, the DD model have a distinct restriction; the model can only be used on GFETs with channel length longer than the mean free path λ [14].

5.2.1 Drift Velocity and New Current Expression

To calculate the current of the model we firstly focus on the last part of equation (5.1), the drift velocity v_{drift}. The drift velocity can be written as

$$v_{drift} = \frac{\mu\mathscr{E}}{1+\frac{\mu|\mathscr{E}|}{v_{sat}}} = \frac{\mu(-\frac{dV}{dx})}{1+\frac{\mu|-\frac{dV}{dx}|}{v_{sat}}}, \tag{5.2}$$

where μ is the mobility, V is the potential in the channel compared to ground, and v_{sat} is the saturation velocity [15, 45]. Substituting the expression from equation (5.2) into equation (5.1) gives

$$I_{ds} = -WQ(x)\frac{\mu\left(-\frac{dV}{dx}\right)}{1+\frac{\mu|-\frac{dV}{dx}|}{v_{sat}}}. \tag{5.3}$$

Upon first glance, the expression seems daunting, but after some re-arrangement and calculations,

$$\begin{aligned}
I_{ds}\left(1+\frac{\mu|\frac{dV}{dx}|}{v_{sat}}\right) &= WQ(x)\mu\left(\frac{dV}{dx}\right),\\
\int_0^L I_{ds}\left(1+\frac{\mu|\frac{dV}{dx}|}{v_{sat}}\right)dx &= \int_0^L WQ(x)\mu\left(\frac{dV}{dx}\right)dx,\\
I_{ds}\left(L+\int_0^L \frac{\mu|\frac{dV}{dx}|}{v_{sat}}dx\right) &= W\int_0^L Q(x)\mu\left(\frac{dV}{dx}\right)dx,\\
I_{ds}\left(L+\left|\int_0^{V_{ds}} \frac{\mu}{v_{sat}}dV\right|\right) &= W\int_0^{V_{ds}} Q(x)\mu dV,
\end{aligned} \tag{5.4}$$

a relatively simple form,

$$I_{ds} = W\frac{\int_0^{V_{ds}} Q(x)\mu dV}{L+\left|\int_0^{V_{ds}} \frac{\mu}{v_{sat}}dV\right|}, \tag{5.5}$$

can be found. The dilemma with equation (5.5) is that the integral is over V, instead of the preferable V_{ch}, which most of our variables have a known dependency on. Because the relationship between V and V_{ch} is well known from equation (4.9), the following replacement

$$dV = dV\frac{dV_{ch}}{dV_{ch}} = dV_{ch}\frac{dV}{dV_{ch}}, \tag{5.6}$$

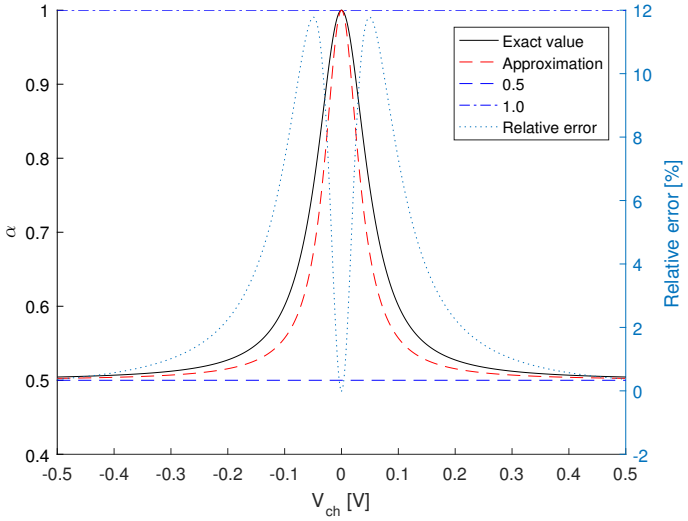

Figure 5.1: The weighting factor α versus the channel potential V_{ch}. The exact expression from equation (4.11) [15] and different approximations [14, 16, 45]. The relative error between the exact expression and the approximation in equation (5.7) is shown, with the scale on the right side.

can be made. However, to be able to calculate the derivative from equation (4.9), the expressions for α and C_q have to be simplified or approximated.

5.2.2 Capacitance Weighting Factor

The capacitance weighting factor α in equation (4.11) has a dependency on V_{ch}. Yet, a static value of either 1 or 0.5 has been used in earlier works [45,47,51]. The exact value of α, from equation (4.11), is shown in figure 5.1 using MATLAB [18]. The value of α goes towards 0.5 for $q|V_{ch}| \gg kT$, on the contrary α goes towards 1 when $q|V_{ch}| \ll kT$. The simple static values $\alpha = 1$ and $\alpha = 0.5$ are shown in the figure. The first gives, as can be seen in figure 5.1, an overestimation for large values of V_{ch}, while the latter gives an underestimation when V_{ch} is small.

To avoid inaccurate results, yet get a simplified expression, Jing et al. [14] suggest the following approximation,

$$\alpha = \left(\frac{1}{1 + c_3 {V_{ch}}^2} + 1 \right) \alpha_{min}, \tag{5.7}$$

where $\alpha_{min} = 0.5$ and the constant is defined as

$$c_3 = \frac{q^2}{(kT \ln(4))^2}. \tag{5.8}$$

Using MATLAB [18], the relative error, between equation (5.7) and equation (4.11), is calculated. The biggest error occurs when E_f and E_d are in close proximity of each other, with maximum value of 11.78% . The relative error becomes almost undistinguishable for large values of $|V_{ch}|$.

5.2.3 Quantum Capacitance

Because of the complexity of equation (4.8) approximations are commonly accepted. Two different approximations as well as the exact value are shown in figure 5.2. A very simple approximation expressed as

$$C_q = 2qc_4|V_{ch}| \tag{5.9}$$

can be used [47], where the constant c_4 is defined as

$$c_4 = \frac{q^2}{\pi(\hbar v_F)^2}. \tag{5.10}$$

However, the approximation in equation (5.9) is inaccurate in the proximity of $V_{ch} = 0$. Another approximation, commonly known as the square-root-based approximation,

$$C_q = \frac{2q^2kT\ln(4)}{\pi(\hbar v_F)^2}\sqrt{1+\left(\frac{qV_{ch}}{kT\ln(4)}\right)^2}, \tag{5.11}$$

can be used to improve the accuracy [51]. The relative error, between the square-root approximation and the exact result, is calculated and displayed with MATLAB [18], the maximum relative error is 7.97%.

5.2.4 dV/dVch

The derivative of equation (4.9) can be written in a simple form if one assumes that capacitance weighting factor $\alpha = 1$ and if one ignores the fact that the quantum capacitance C_q depends on V_{ch}. This gives the expression

$$\frac{dV}{dV_{ch}} = 1 + \frac{C_q(V_{ch})}{C_{ox-top} + C_{ox-back}}. \tag{5.12}$$

If one instead uses equation (5.7) for α and the square-root approximation in equation (4.8) for C_q substituted into equation (4.9), the derivative can be expressed as

$$\frac{dV}{dV_{ch}} = 1 + \frac{c_5\alpha_{min}\left(2 + c_3{V_{ch}}^2\left(3 + 2c_3{V_{ch}}^2\right)\right)}{\left(1 + c_3{V_{ch}}^2\right)^{\frac{3}{2}}}. \tag{5.13}$$

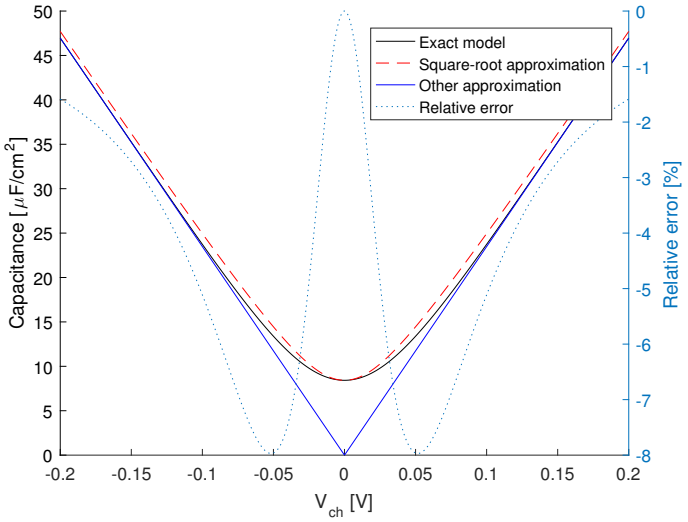

Figure 5.2: Quantum capacitance C_q. Exact value, square-root approximation [51] as well as a second approximation [16]. The relative error between the exact expression in equation (4.8) *and the approximation in equation* (5.11) *is shown, with the scale on the right side.*

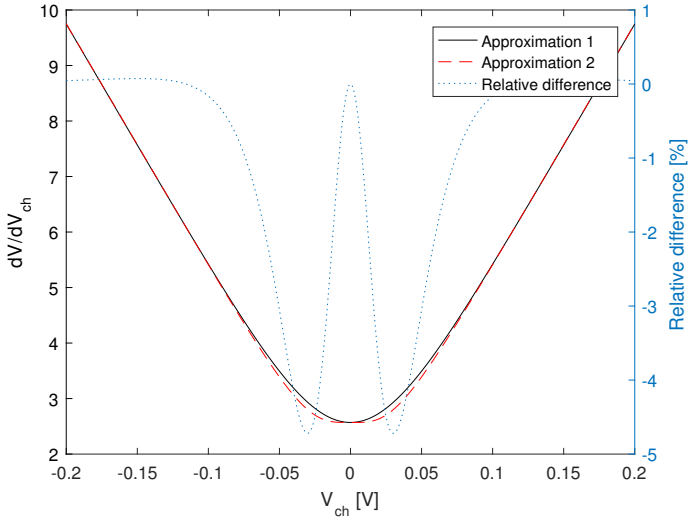

Figure 5.3: Two approximations for dV/dV_{ch}. Approximation 1 corresponds to equation (5.12)*, while Approximation 2 corresponds to equation* (5.13)*. The relative difference is shown, with the scale on the right side.*

Where the definition of c_3 is shown in equation (5.8) and c_5 is defined as

$$c_5 = \frac{2q^2 kT \ln(4)}{(C_{ox-top} + C_{ox-back})\,\pi(\hbar v_F)^2}. \tag{5.14}$$

Equations (4.6) and (4.7) show further details about C_{ox-top} and $C_{ox-back}$. A comparison of the two approximations for dV/dV_{ch} from equations (5.12) and (5.13) are shown in figure 5.3. The figure shows that the biggest difference occurs in the vicinity of $V_{ch} = 0$, with maximum value -4.7%.

5.2.5 Carrier Density

There are three important parameters that have not been discussed yet: Q(x), μ and v_{sat}. The net mobile sheet charge density Q_{net} can be used as the charge carrier density, and is expressed as

$$Q_{net} = |q(p - n)|. \tag{5.15}$$

Equation (5.15) is useful for conventional field-effect transistors (FETs). However, this approximation underestimates the carrier density for when E_f and E_d are in close proximity, because holes and electrons in graphene both additively contribute to the overall current, as discussed in *Section 4.2.2 Biasing Configurations*. Accurate result is therefore only given from equation (5.15) when $q|V_{ch}| \gg kT$. The charge density relevant for transport,

$$Q_t = q(p + n), \tag{5.16}$$

can be used as a mean to improve the model [51]. Equation (5.16) goes towards equation (5.15) when $q|V_{ch}| \gg kT$, but gives a better approximation for small values of V_{ch}. Figure 5.4 shows a comparison of equations (5.15) and (5.16).

Using the exact expression for Q_t demands calculations of n and p with the Fermi-Dirac integral, which is not completely trivial. A simplification proposed by Parrish et al. [51] can be written as

$$Q_t \approx \frac{q\pi(kT)^2}{3(\hbar v_F)^2} + \frac{q^3 {V_{ch}}^2}{\pi(\hbar v_F)^2}, \tag{5.17}$$

and will be used in this report. The simplification shows good agreement with the exact data, see figure 5.5. The maximum relative error is only 0.0001%.

Another constant is introduced, to simplify for later calculations:

$$c_6 = \frac{\pi(kT)^2}{3(\hbar v_F)^2}, \tag{5.18}$$

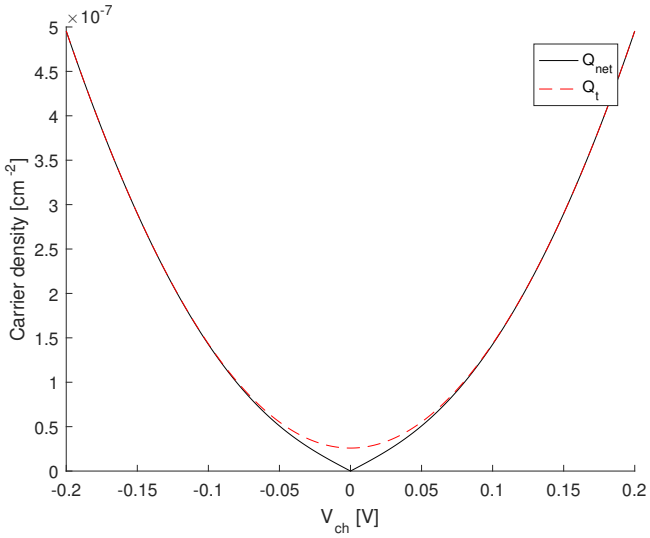

Figure 5.4: The net mobile sheet charge density Q_{net} compared with the charge density relevant for transport Q_t.

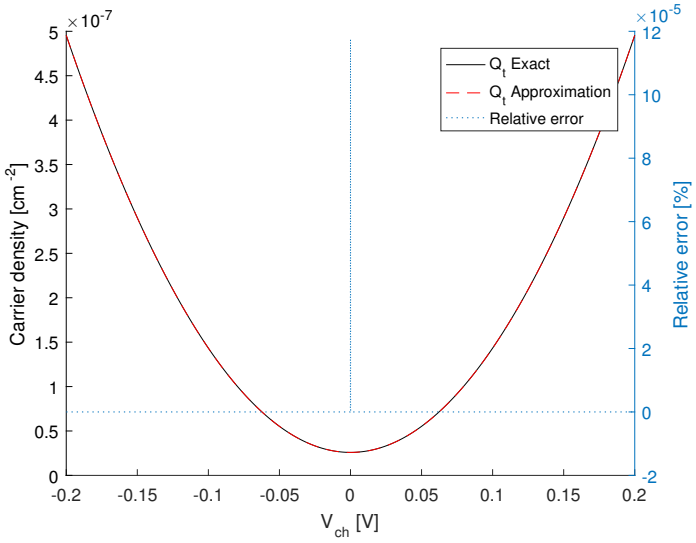

Figure 5.5: Charge density relevant for transport Q_t, comparing equations (5.16) *and* (5.17)*. Relative error scale is shown on the right side.*

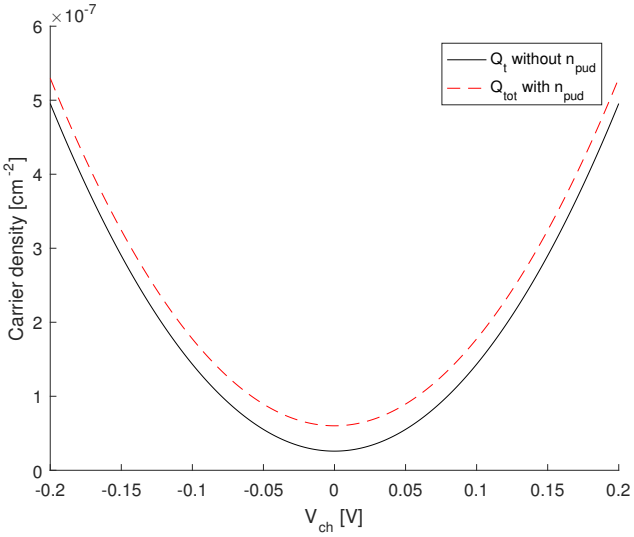

Figure 5.6: Comparison between the Q_t and Q_{tot} from equations (5.19) *and* (5.21).

Together with c_4 in equation (5.10) this gives the very short expression

$$Q_t = q(c_6 + c_4 {V_{ch}}^2). \tag{5.19}$$

Finally, the residual charge density known as electron-hole puddles,

$$n_{pud} = \frac{\Delta^2}{\pi(\hbar v_F)^2} \tag{5.20}$$

where Δ is the spatial inhomogeneity of potential resulting in the puddles [15], has to be added to the expression. This gives

$$Q_{tot} = q(c_6 + c_4 {V_{ch}}^2 + n_{pud}). \tag{5.21}$$

5.2.6 Mobility

The second undefined parameter, is the mobility μ. The effective carrier mobility μ_{eff} is defined as

$$\mu_{eff} = \frac{n\mu_n + p\mu_p + n_{pud}\left(\frac{\mu_n+\mu_p}{2}\right)}{n + p + n_{pud}}, \tag{5.22}$$

where μ_n and μ_p are the low field mobilities for electrons and holes. However, the fact that the mobility decreases with increased carrier density also has to

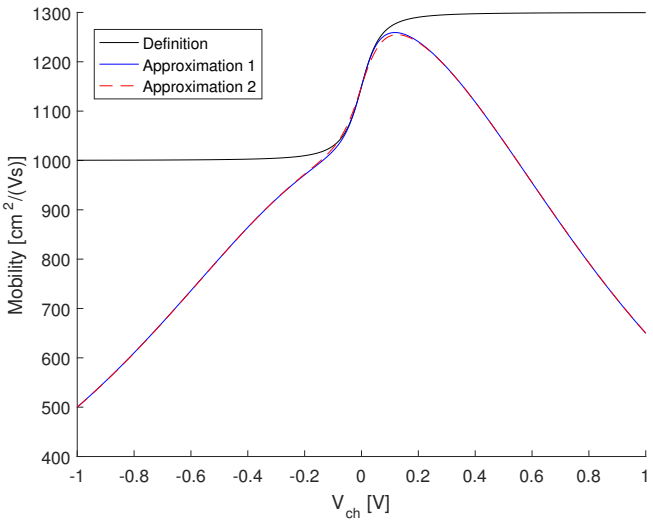

Figure 5.7: Comparison between different approximations for the effective mobility μ_{eff}. The definition from equation (5.22) is shown in comparison with Approximation 1 from equation (5.23) [14] as well as the more practical Approximation 2 from equation (5.25) [55].

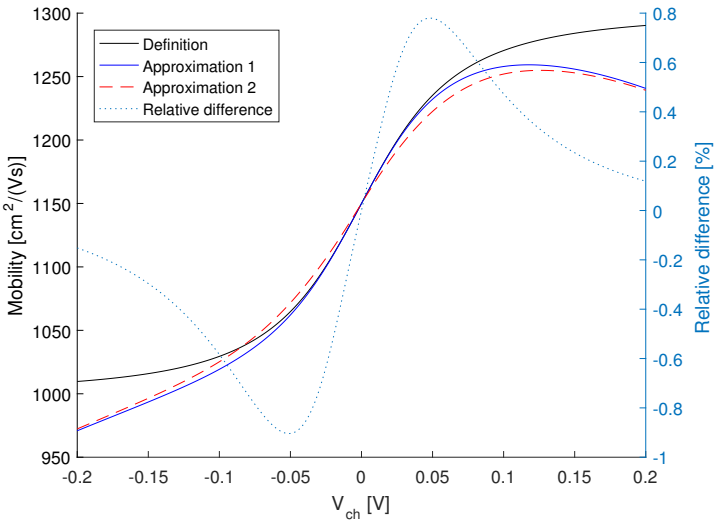

Figure 5.8: Enlargment of figure 5.7, comparing different approximations for the effective mobility μ_{eff}. The definition from equation (5.22) is shown in comparison with Approximation 1 from equation (5.23) [14] as well as the more practical Approximation 2 from equation (5.25) [55]. The relative difference between Approximation 1 and 2 is shown, with the scale on the right side

be taken into consideration. An added factor such as

$$\mu_{eff} = \frac{n\mu_n + p\mu_p + n_{pud}\left(\frac{\mu_n+\mu_p}{2}\right)}{n + p + n_{pud}} \left(\frac{s}{s + {V_{ch}}^2}\right), \tag{5.23}$$

give better agreement with reality [55]. s is in the unit the square of the reference channel potential, used as an empirical fitting parameter. Once again, we want to avoid complicated calculations and instead have a dependency on V_{ch}, as this will help us for future calculations. A simplification for μ_{np} is suggested by Dorgan et al. [55] and can be written as follows

$$\mu_{np} = \left(\frac{14(\mu_p - \mu_n)V_{ch}}{\sqrt{1 + c_3{V_{ch}}^2}} + \frac{\mu_p + \mu_n}{2}\right). \tag{5.24}$$

Together with the approximated expression for $(n + p)$, in equation (5.19), the expression

$$\mu_{eff} = \left(\frac{14(\mu_p - \mu_n)(c_6 + c_4{V_{ch}}^2)V_{ch}}{(c_6 + c_4{V_{ch}}^2 + n_{pud})\sqrt{1 + c_3{V_{ch}}^2}} + \frac{\mu_p + \mu_n}{2}\right)\left(\frac{s}{s + {V_{ch}}^2}\right) \tag{5.25}$$

is derived. The constants are defined in equations (5.8), (5.10) and (5.18). The expressions for mobility in equations (5.22), (5.23) and (5.25) are shown in figures 5.7 and 5.8. The relative difference between equations (5.23) and (5.25) is also shown. The biggest difference occurs in the proximity of $V_{ch} = 0$ with the value 0.9% .

5.2.7 Velocity Saturation

Finally the third variable, v_{sat} is reviewed. Velocity saturation is assumed to be caused by scattering of phonons, once the carrier reaches a specific energy threshold, it will immediately scatter [56]. In some literature [16, 47], v_{sat} has been modelled as being constant, for example as

$$v_{sat} = \frac{2v_F}{\pi}. \tag{5.26}$$

However, the velocity saturation changes with V_{ch}, as we know from *Section 4.3 Negative Differential Resistance*. Therefore, other approximations of v_{sat} have to be used to accurately represent this dependency. To model v_{sat} as being inversely proportional to V_{ch} has been fairly popular. A fitting parameter is often added to improve the accuracy of the model [16, 51, 56]. One simple

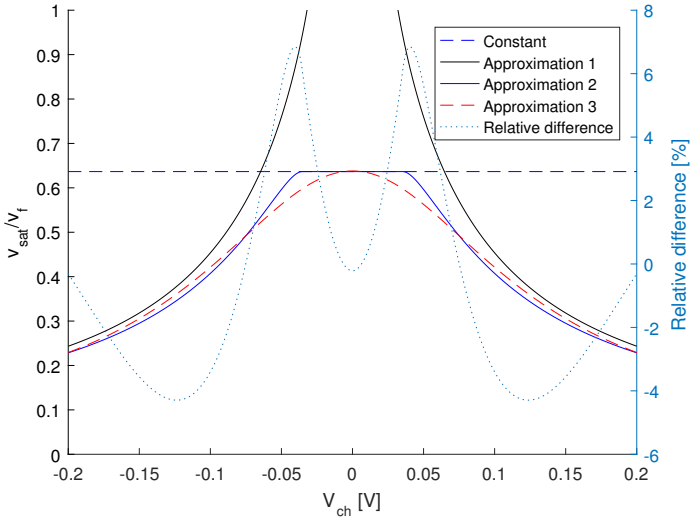

Figure 5.9: Four approximations for v_{sat}. The constant approximation corresponds to equation (5.26) [16], Approximation 1 corresponds to equation (5.27) [16, 51, 56], Approximation 2 corresponds to equation (5.28) [15, 57] and finally the continuous function in Approximation 3 corresponds to equation (5.29) [14]. The relative difference between Approximation 2 and 3 is shown, with the scale on the right side.

example, without a fitting parameter, is

$$v_{sat} = \frac{\hbar\Omega}{\hbar\sqrt{\frac{\pi Q_{net}}{q}}}, \tag{5.27}$$

where $\hbar\Omega$ is the optical phonon energy [16, 51, 56]. Equation (5.27) provides good results for high values of $|V_{ch}|$, but goes to infinity as V_{ch} goes towards zero, giving unrealistic values. A two-region model such as,

$$v_{sat} = \begin{cases} \frac{2q\Omega}{\pi^2\hbar v_F Q_{net}}\sqrt{\frac{\pi Q_{net}(\hbar v_F)^2}{q} - \left(\frac{\hbar\Omega}{2}\right)^2}, & \text{when } |Q_{net}| \geq q\frac{\Omega^2}{2\pi {v_F}^2}, \\ \frac{2v_F}{\pi}, & \text{when } |Q_{net}| < q\frac{\Omega^2}{2\pi {v_F}^2}, \end{cases} \tag{5.28}$$

can be used to avoid the inaccuracy in the proximity of $V_{ch} = 0$ [15,57]. However, a two-region model is not optimal since it causes problems, for example by giving discontinuities in g_m. A continuous model that does not go to infinity would be optimal. The approximation

$$v_{sat} = v_F\left(\frac{\frac{v_{sat}(\max) - v_{sat}(\min)}{v_F}}{1 + c_7 {V_{ch}}^2} + \frac{v_{sat}(\min)}{v_F}\right), \tag{5.29}$$

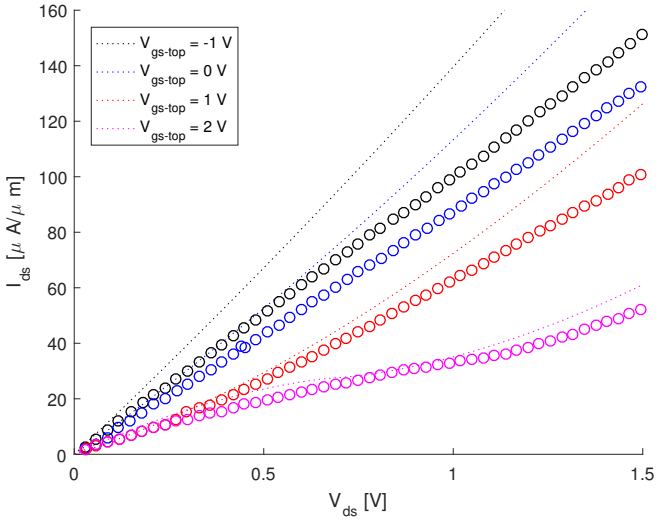

Figure 5.10: Drain-to-source current I_{ds} versus drain-to-source potential V_{ds} shown for both measured data provided by Wang et al. [32] and DD model derived from equation (5.33).

where

$$c_7 = \left(\frac{q}{5kT}\right)^2, \tag{5.30}$$

gives reasonable results with a continuous function [14]. Figure 5.9 shows a comparison between the approximations. The relative difference between equations (5.28) and (5.29) is visible with the scale on the right side. The difference is biggest when E_d and E_f are in close proximity with each other, with the maximum difference 6.84%.

5.2.8 Simulation Model 1

My first simulation model begins with the expression described in equation (5.5). The model assumes that the mobility is not dependent on the potential, in the same manner as has been done by Jiménez [47]. Furthermore, v_{sat} is also said to be independent on the potential, as in equation (5.26). This means that the expression can be simplified

$$I_{ds} = \frac{\mu W \int_0^{V_{ds}} Q(x)dV}{L + \mu \frac{\pi |V_{ds}|}{2v_F}}. \tag{5.31}$$

We then use the simplified version of dV/dV_{ch} described in equation (5.12), which gives an expression that can be written as

$$I_{ds} = \frac{\mu W \int_{V_{ch-drain}}^{V_{ch-source}} Q(x)\left(1 + \frac{C_q}{C_{ox-top}+C_{ox-back}}\right) dV_{ch}}{L + \mu\frac{\pi|V_{ds}|}{2v_F}}. \tag{5.32}$$

The relative simple expression for the quantum capacitance in equation (5.9) is used, together with the final expression for the carrier density in equation (5.21), the expression can be written as

$$I_{ds} = \frac{\mu W \int_{V_{ch-drain}}^{V_{ch-source}} \left(q(c_6 + c_4 {V_{ch}}^2 + n_{pud})\right) \frac{2qc_4|V_{ch}|}{C_{ox-top}+C_{ox-back}} dV_{ch}}{L + \mu\frac{\pi|V_{ds}|}{2v_F}}. \tag{5.33}$$

This expression gives the following numerator integral

$$\begin{aligned} & q\Big((c_6 + n_{pud}) \left(V_{ch} + \frac{qc_4}{C_{ox-top} + C_{ox-back}} {V_{ch}}^2 \operatorname{sgn}(V_{ch}) \right) \\ & + c_4 \left(\frac{{V_{ch}}^3}{3} + \frac{qc_4}{2(C_{ox-top} + C_{ox-back})} {V_{ch}}^4 \operatorname{sgn}(V_{ch}) \right) \Big) \Big|_{V_{ch-drain}}^{V_{ch-source}} . \end{aligned} \tag{5.34}$$

The model have been implemented in Verilog-A and run with the simulation program ADS [17]. A comparison between the model and actual measured data by Wang et al. [32] is shown in figure 5.10. The following parameter values

$$L = 5\ \mu\text{m}, \tag{5.35}$$
$$W = 1\ \mu\text{m}, \tag{5.36}$$
$$t_{ox-top} = 15\ \text{nm}, \tag{5.37}$$
$$t_{ox-back} = 300\ \text{nm}, \tag{5.38}$$
$$\varepsilon_{ox-top} = 8.9, \tag{5.39}$$
$$\varepsilon_{ox-back} = 3.9, \tag{5.40}$$
$$V_{gs-back} = 0\ \text{V}, \tag{5.41}$$
$$V_{dirac-0-top} = 1.1\ \text{V}, \tag{5.42}$$
$$V_{dirac-0-back} = 11\ \text{V}, \tag{5.43}$$
$$R_{source} = 2\ \text{m}\Omega, \tag{5.44}$$
$$R_{drain} = 2\ \text{m}\Omega, \tag{5.45}$$
$$\mu_n = 920\ \text{cm}^2/(\text{Vs}), \tag{5.46}$$
$$\mu_p = 1330\ \text{cm}^2/(\text{Vs}), \tag{5.47}$$
$$\Delta = 0.092\ \text{V}^2, \tag{5.48}$$

are used in the simulation, all of which are extracted from the measured data by Wang et al. [32]. V_{gs-top} have four different values; -1,0,1 and 2 V as shown in the figure. The mobility is assumed to be constant in this simple simulation model and is taken as a average between the hole and electron mobility.

5.2.9 Simulation Model 2

In this simulation model we start by making the same assumptions as in *Section 5.2.8 Simulation Model 1*; the mobility μ is independent of the potential, the velocity saturation v_{sat} is said to be constant as in equation (5.26) and dV/dV_{ch} is described by equation (5.12). This gives us the same expression as in equation (5.32). However, moving forward we use the more accurate square-root approximation in equation (5.11) for the quantum capacitance C_q. The following expression is obtained

$$I_{ds} = \frac{\mu W \int_{V_{ch-drain}}^{V_{ch-source}} Q(x)\left(1 + \frac{\frac{2q^2 kT\ln(4)}{\pi(\hbar v_F)^2}\sqrt{1+\left(\frac{qV_{ch}}{kT\ln(4)}\right)^2}}{C_{ox-top}+C_{ox-back}}\right) dV_{ch}}{L + \mu\left|\int_0^{V_{ds}} \frac{1}{v_{sat}(V_{ch})} dV\right|}. \tag{5.49}$$

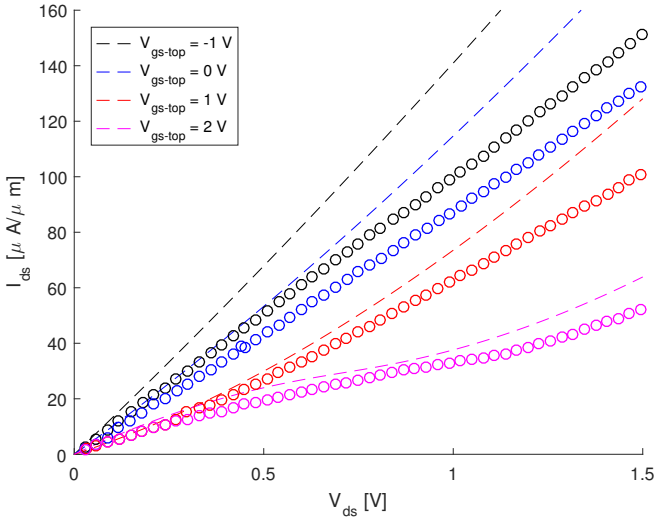

Figure 5.11: Drain-to-source current I_{ds} versus drain-to-source potential V_{ds} shown for both measured data provided by Wang et al. [32] and DD model derived from equation (5.49).

The numerator integral can then be calculated analytically, which gives

$$\frac{qc_4}{3}{V_{ch}}^3 - \frac{c_8}{8(c_3)^{3/2}}\operatorname{arcsinh}\left(\sqrt{c_3}V_{ch}\right) + \sqrt{1+c_3{V_{ch}}^2}\left(\frac{c_8}{8c_3}V_{ch} + \frac{c_8}{4}{V_{ch}}^3\right)\Bigg|_{V_{ch-drain}}^{V_{ch-source}} + q\left(c_6 + n_{pud}\right)V_{ds} \tag{5.50}$$

where the constants are defined as equations (5.8), (5.10) and (5.18) as well as

$$c_8 = \frac{1}{C_{ox-top} + C_{ox-back}} \cdot \frac{2q^5 kT\ln(4)}{\pi^2(\hbar v_F)^4}. \tag{5.51}$$

The model is implemented in Verilog-A and run using the simulation program ADS [17]. The same parameter values as in *Section 5.2.8 Simulation Model 1*, equations (5.35)–(5.48) are used, with the result shown in figure 5.11.

5.2.10 Simulation Model 3

In this section we derive a simulation model that uses the most the more precise approximations described in previous sections. The mobility is therefore not assumed to be independent of the potential, but instead as described in

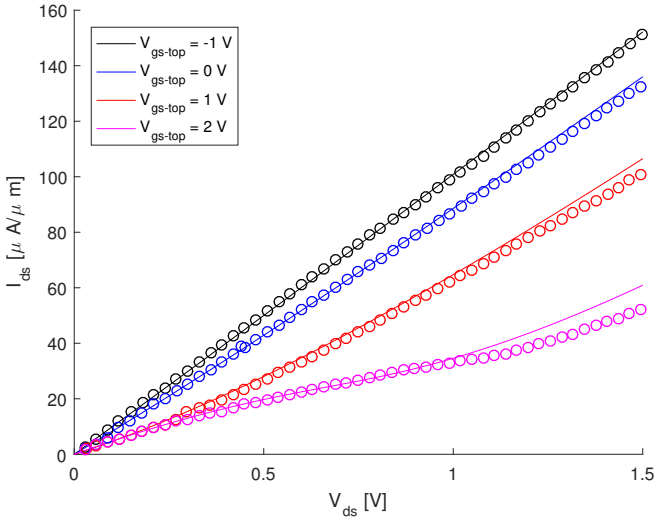

Figure 5.12: Drain-to-source current I_{ds} versus drain-to-source potential V_{ds} shown for both measured data provided by Wang et al. [32] and DD model derived from equations (5.53) *and* (5.54).

equation (5.25). Equation (5.13) is substituted into equation (5.5) which gives

$$I_{ds} = W \frac{\int_{V_{ch-drain}}^{V_{ch-source}} Q\mu \left(1 + \frac{c_5 \alpha_{min}\left(2+c_3 {V_{ch}}^2 \left(3+2c_3 {V_{ch}}^2\right)\right)}{\left(1+c_4 {V_{ch}}^2\right)^{\frac{3}{2}}}\right) dV_{ch}}{L + \left| \int_{V_{ch-drain}}^{V_{ch-source}} \frac{\mu}{v_{sat}} \left(1 + \frac{c_5 \alpha_{min}(2+c_3 {V_{ch}}^2 (3+2c_3 {V_{ch}}^2))}{(1+c_4 {V_{ch}}^2)^{\frac{3}{2}}}\right) dV_{ch} \right|}. \tag{5.52}$$

Substituting equations (5.21), (5.25) and (5.29) into equation (5.52) gives an expression, with the numerator

$$\begin{aligned} & W \int_{V_{ch-drain}}^{V_{ch-source}} \left(q(c_6 + c_4 {V_{ch}}^2 + n_{pud})\right) \\ & \cdot \left(\frac{14(\mu_p - \mu_n)(c_6 + c_4 {V_{ch}}^2) V_{ch}}{(c_6 + c_4 {V_{ch}}^2 + n_{pud})\sqrt{1 + c_3 {V_{ch}}^2}} + \frac{\mu_p + \mu_n}{2} \right) \left(\frac{s}{s + {V_{ch}}^2} \right) \\ & \cdot \left(1 + \frac{c_5 \alpha_{min} \left(2 + c_3 {V_{ch}}^2 \left(3 + 2c_3 {V_{ch}}^2\right)\right)}{\left(1 + c_4 {V_{ch}}^2\right)^{\frac{3}{2}}} \right) dV_{ch}. \end{aligned} \tag{5.53}$$

and the denominator

$$L + \left| \int_{V_{ch-drain}}^{V_{ch-source}} \frac{\left(\frac{14(\mu_p - \mu_n)(c_6 + c_4 {V_{ch}}^2) V_{ch}}{(c_6 + c_4 {V_{ch}}^2 + n_{pud})\sqrt{1 + c_3 {V_{ch}}^2}} + \frac{\mu_p + \mu_n}{2} \right) \left(\frac{s}{s + {V_{ch}}^2} \right)}{v_F \left(\frac{\frac{v_{sat}(\max) - v_{sat}(\min)}{v_F}}{1 + c_7 {V_{ch}}^2} + \frac{v_{sat}(\min)}{v_F} \right)} \right| \cdot \left| \left(1 + \frac{c_5 \alpha_{min} \left(2 + c_3 {V_{ch}}^2 \left(3 + 2 c_3 {V_{ch}}^2 \right) \right)}{\left(1 + c_4 {V_{ch}}^2 \right)^{\frac{3}{2}}} \right) dV_{ch} \right|. \tag{5.54}$$

To simplify the calculation of the expression we assume is assumed that V_{ch} for n_{pud} is the average value of $V_{ch-drain}$ and $V_{ch-source}$, the same approximation has been made by Jing et al. [14]. The expression is solved analytically and implemented in Verilog-A. A simulation is made using ADS [17]. Figure 5.12 shows a comparison between measured data, from Wang et al. [32], and the simulated DD model from equations (5.53) and (5.54). The same parameter values as in *Section 5.2.8 Simulation Model 1*, equations (5.35)–(5.48) are used.

5.3 Virtual Source Model

The model described in this section focuses on ballistic transport and is therefore applicable for shorter channels where the ballistic transport is dominant. However, adjustments can be made to the model so that it works also in the diffusive regime.

The VS model is an alternative transport model based on the concept of one (or several) virtual source(s). The height of the VS modulates the number of charge carriers injected. All carriers that exceed the potential of the VS are said to travel ballistically to the other terminal with a drift velocity in accordance with the potential difference between source and drain V_{ds} [4, 25, 32].

For graphene this means that a positive drain-to-source potential V_{ds} will create an electric field that makes holes travel from drain to source, while electrons will travel from source to drain. According to the VS model, the electrons that are injected from the source with energies higher than the VS at source, travel ballistically through the channel to the drain side. Simultaneously, holes injected from the drain side, with energies lower than the VS at source, will travel ballistically to the source side. Both electrons and holes contribute to the drain-to-source current I_{ds}. The carriers that cannot pass the barrier on their respective side are reflected back [4, 48, 52].

The principle for ballistic transport starts off the same way as any other long channel GFETs. The gate voltages electrostatics controls the charge density at the virtual sources. The concentrations at the virtual sources can be calculated

as [4, 32, 48]

$$Q_{VS-elec} = C_{ox-top} c_9 \phi_t \ln\left(1 + e^{\frac{V_{gs}-V_{t-elec}}{c_9\phi_t}}\right) + Q_{dis}, \tag{5.55}$$

$$Q_{VS-hole} = C_{ox-top} c_9 \phi_t \ln\left(1 + e^{\frac{V_{gs}+V_{t-hole}}{c_9\phi_t}}\right) + Q_{dis},, \tag{5.56}$$

where V_{t-elec} and V_{t-hole} can be found by solving

$$V_{t-elec} = V_{dirac-0-top} - c_{10}\phi_t \frac{1}{1 + e^{\frac{V_{gs}-\left(V_{t-elec}-\frac{c_{10}\phi_t}{2}\right)}{\frac{c_{10}\phi_t}{2}}}}, \tag{5.57}$$

$$V_{t-hole} = V_{dirac-0-top} - c_{10}\phi_t \frac{1}{1 + e^{\frac{V_{gs}+\left(V_{t-hole}+\frac{c_{10}\phi_t}{2}\right)}{\frac{c_{10}\phi_t}{2}}}}.. \tag{5.58}$$

Some clarification regarding the notations are in order; Q_{dis} is the charge density as a result of electron-hole puddles, both c_{10} and c_9 are related to the sub-threshold, and ϕ_t is the thermal voltage defined as

$$\phi_t = \frac{kT}{q}. \tag{5.59}$$

Q_{dis}, c_9, c_{10} and the oxide thickness t_{ox-top} are fitting parameters that have to be adjusted to experimental data or numerical calculations, for each simulation [32, 48].

Calculation of the drift velocity can be done in a similar manner as for the DD model. Rakheja et al. [48] presents the following equation

$$\begin{aligned} v_{drift} &= \frac{V_{ds}\mu}{L\left(1 + \left(\frac{V_{ds}}{v_{sat}}\right)^{\beta}\right)^{\frac{1}{\beta}}}, \\ &= \frac{V_{ds}\mu}{L\left(1 + \left(\frac{V_{ds}\mu}{v_{VS0}L}\right)^{\beta}\right)^{\frac{1}{\beta}}} \end{aligned} \tag{5.60}$$

The expression is presented in a different manner but contains the same components; a dependency on the mobility μ and the velocity saturation v_{sat}. L is the length of the transistor channel, v_{VS0} is the carrier injection velocity at the virtual source and β is a fitting parameter. The injection velocity and mobility are the same for both holes and electrons [48]. Instead a contact resistances are used as a means to compensate for the different behaviours in the hole and electron branch. $R_{hole} < R_{elec}$ for when the hole transport is larger [4].

What is interesting with this approximation is that the final current expres-

sion

$$I_{ds} = W(Q_{VS-elec} + Q_{VS-hole})v_{drift}, \tag{5.61}$$

can be found in a relatively simple manner.

5.3.1 Simulation Model 4

The final simulation model is implemented in Verilog-A and run using ADS [17]. The parameters used are taken from Rakheja et al. [48] or the parameter is assumed to be the same as for the other simulations.

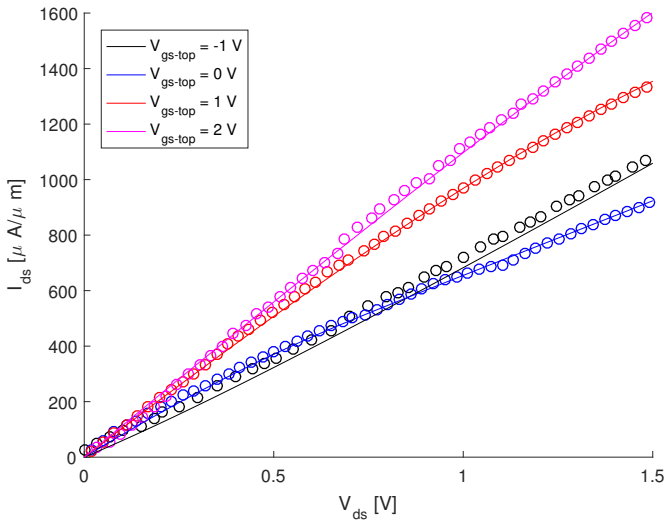

Figure 5.13: Drain-to-source current I_{ds} versus drain-to-source potential V_{ds} shown for both measured data provided by Rakheja et al. [48] and VS model derived from equation (5.61).

Chapter 6

Discussion of Result

I realised, already at the beginning of my thesis work, that there was a lack of fundamental explanations for the advanced simulation models used for graphene field-effect transistors (GFETs). Graphene and GFETs are relatively new fields, so it is not peculiar that there is room for improvement and that the educational material is sparse at some levels.

Simultaneously, researchers try to push the limits and be first in discovering the next revolutionary step for graphene. This means that there is an abundance of advanced articles to read, but not much that cover the fundamentals. I want to note that we cannot expect articles to explain every detail as most publisher have strict length limits. But I still find it rather discouraging that the reader is assumed to have a deep understanding of not only electronics, but also physics, quantum mechanics, mathematics and fabrication processes. That is why I decided to put a large emphasis on the theory behind GFETs, maybe it could make more people discover the interesting fields of graphene and GFETs.

If the fundamental knowledge is missing, I experienced that it is demanding to understand why some simulation models are more or less accurate. That every author seems to claim that their model is as accurate as it can get does not make it any easier. On several occasions, [14–16, 32, 47, 53] authors use another person's findings together with their own improvements. However, I have from time to time encountered articles where it seems like the author has not fully understood the theory from the previous author, on which they are now building their model.

Furthermore, if a basic understanding is missing, notations and terms can get lost and mixed together, which means that two simulation models can have the same terms, yet mean different things. For example, Rakheja et al. [48] present a simulation model that has the parameter Q_{dis}. This parameter is said to describe the electron-hole puddles, which has been denoted as n_{pud} in other

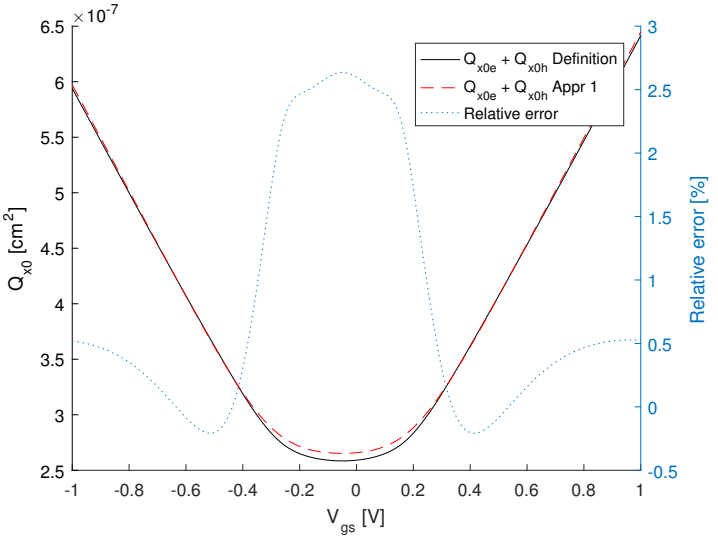

Figure 6.1: Comparison between the charge density $Q_{VS-elec}$ and $Q_{VS-hole}$ from equations (5.55) *and* (5.56) *[48], and the charge density in equations* (4.2) *and* (4.3).

simulation models [15, 16]. However, in the former model the parameter is also used as a fitting parameter, which means that it has to be adjusted. For me, that is something that is likely to create confusion.

When I started my thesis work, my first choice was to look at the virtual source (VS) model since it works even in the ballistic regime. However, the model did not succeed in showing negative differential resistance (NDR). The next question therefore became why did it not showcase NDR. As described in this report, the theory behind NDR has been under debate and different theories have been put forward. Again, I felt like the fundamental knowledge was missing. I therefore decided to not only research the theory behind graphene and GFETs, but also to look at the more commonly used drift-diffusion (DD) model that I know manages to showcase NDR.

Comparing the VS model with the DD model is complicated. A simple comparison is shown in figure 6.1. The values of Q_{dis}, c_9, c_{10} and t_{ox-top} have been adjusted according to the model by Rakheja et al. [48] and the value of n_{pud} has been set so that the two graphs give good agreement. We can see that the graphs have a relatively similar shape which can give us an indication that the calculations of the charge carrier density are done in an equivalent manner.

Therefore, to get a better understanding of NDR, I decided to investigate what parameters, in the DD model, are important for the NDR. My hypothesis was that if I made too large approximations in the parameters such as the

velocity saturation, the NDR would not be visible. However, all DD models showed NDR. The only simulation that did not show NDR was the VS model. This behaviour is somewhat peculiar as I was expecting NDR not to be visible on the account of the explanation from Sharma et al. [38], see *Section 4.3 Negative Differential Resistance*. However, due to a mishap in my programming, I did some simulations where the drain-to-source voltage V_{ds} in the denominator was set to 1. For those instances, NDR was not present. Unfortunately, since the equation have been re-written, it is not simple to draw any type of conclusion from what that means for the physical device.

Going through the different parameters in the DD model, to see what approximations are made, was an important part of my work. It gave me a good insight into what approximations have been made successfully in earlier works as well as a good understanding of the physics behind the GFET. The relative error differed from 11.78% for the weighting factor, see figure 5.1, to as little as 0.0001% for the charge density relevant for transport, see figure 5.5. Most parameters yield inaccuracy, particularly in the vicinity of the Dirac point, so that for small values of $|V_{ch}|$, the model is inaccurate. As a consequence, under certain biasing conditions, analogue properties are altered, which can drastically affect the outcome of the circuit design. The approximation improvements in *Section 5.2 Drift-Diffusion Model* all look minuscule, but together they amount in a big difference for the end result, as can be seen in figure 5.10.

In figure 6.2, the three DD models are shown in the same graph. It is quite arduous to see, but the second simulation model in *Section 5.2.9 Simulation Model 2* actually give less accurate result than the simple first simulation model in *Section 5.2.8 Simulation Model 1*. This is because the first model overestimates dV/dV_{ch} while C_q is underestimated. This means that these two parameters actually help to compensate each other, giving a more accurate end result. If we use the most accurate approximation of C_q, as in simulation model 2, there is no compensation and the result give a greater overestimation. Overall we can see that the denominator is too small for the first two simulations since v_{sat} is overestimated, as can bee seen in figure 5.9.

The DD model was pleasant to work with as most parameters have a clear physical meaning. This also makes it easier for users who are interested in using the model, rather than understanding all of its different aspects. On the other hand, the DD model does not consider particles that travel ballistically. Even though the model gives good agreement with data, one should expect it to fail for smaller resistor lengths. Ballistic transport is extremely important as the channel length continues to decrease, which is one of the reasons why I wanted to focus also on other models than the DD model. Unfortunately, from my experience, the VS model is much more complex to use. To be able to use the

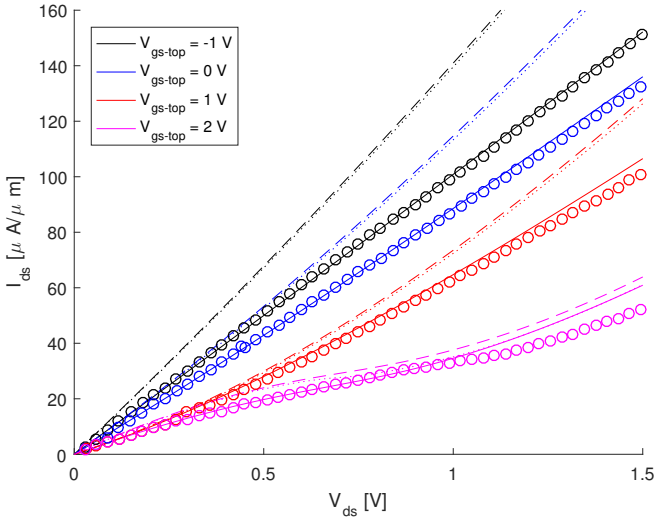

Figure 6.2: Drain-to-source current I_{ds} versus drain-to-source potential V_{ds} shown for both measured data provided by Wang et al. [32] and three different DD models. Model from Section 5.2.8 Simulation Model 1 is shown with dotted. Model from Section 5.2.9 Simulation Model 2 is shown with dashed lines. The last model from Section 5.2.10 Simulation Model 3 is shown with sold lines.

model, experimental data as well as numerical calculations are needed to match with the simulation data. The model needs improvement and a reduction in the amount of fitting parameters. I think that if the theory was studied further, with the knowledge that I have gained from the DD model, the reason why NDR is not visible would become clear.

6.1 Further Work

I believe that, for this field to continue to develop, the fundamental knowledge of all the different properties of graphene and GFETs is crucial. From this, we will be able to understand what assumptions we make and why they fail or work. For future work, I believe that the VS model should be investigated further. I think the model has good potential, especially since it can be adjusted to function both in the diffusive and ballistic regime. Like I mentioned before, I think fewer fitting parameters with clearer physical meaning is central in future work.

Appendices

Appendix A

Graphene energy dispersion using tight-binding approximation

The following Appendix describes in detail how to calculate the energy dispersion of graphene using the tight-binding approximation. The tight-binding approximation assumes that the electronic wavefunction is well approximated by a sum of atomic orbitals. Since graphene is described as a triangular Bravais lattice with a base of two atoms the final wavefunction is made out of two normalised orbital bases

$$\psi = C_A\psi_A + C_B\psi_B. \tag{A.1}$$

Each one can be written as

$$\psi_A = \frac{1}{\sqrt{N}} \sum_A e^{2\pi i \boldsymbol{k}\cdot\boldsymbol{r}_A} \phi_A(\boldsymbol{r} - \boldsymbol{r}_A), \tag{A.2}$$

and

$$\psi_B = \frac{1}{\sqrt{N}} \sum_B e^{2\pi i \boldsymbol{k}\cdot\boldsymbol{r}_A} \phi_B(\boldsymbol{r} - \boldsymbol{r}_B). \tag{A.3}$$

ψ_A has a sum of all the atomic orbitals belonging to the group of lattice points named A, see figure 2.2. ψ_B on the other hand has the sum over the lattice points B, see figure 2.2.

The Hamiltonian operator is used in quantum mechanics and corresponds to the total energy of a system. It can be written as

$$H\psi = E\psi, \tag{A.4}$$

where E is the eigen energy of the system [6, 58]. To calculate E the equation is modified as follows

$$\begin{aligned} \psi^* H\psi &= \psi^* E\psi \\ \int \psi^* H\psi \, d\tau &= \int \psi^* E\psi \, d\tau \\ \int \psi^* H\psi \, d\tau &= E \int \psi^* \psi \, d\tau, \end{aligned} \tag{A.5}$$

where the integral calculated over all space. From this the estimated expectation value of the energy E can be calculated as

$$E = \frac{\int \psi^* H\psi \, d\tau}{\int \psi^* \psi \, d\tau}. \tag{A.6}$$

Substituting the expression from equation (A.1) gives

$$E = \frac{\int (C_A\psi_A + C_B\psi_B)^* H(C_A\psi_A + C_B\psi_B) \, d\tau}{\int (C_A\psi_A + C_B\psi_B)^* (C_A\psi_A + C_B\psi_B) \, d\tau}. \tag{A.7}$$

Next, the expressions in equations (A.2) and (A.3) are added

$$E = \frac{C_A^* C_A \int \psi_A^* H\psi_A \, d\tau + C_A^* C_B \int \psi_A^* H\psi_B \, d\tau + C_B^* C_B \int \psi_B^* H\psi_B \, d\tau + C_B^* C_A \int \psi_B^* H\psi_A \, d\tau}{C_A^* C_A \int \psi_A^* \psi_A \, d\tau + C_A^* C_B \int \psi_A^* \psi_B \, d\tau + C_B^* C_B \int \psi_B^* \psi_B \, d\tau + C_B^* C_A \int \psi_B^* \psi_A \, d\tau}. \tag{A.8}$$

The widely used notation of

$$\int \psi_J^* \psi_I \, d\tau = \langle \psi_J^* | \psi_I \rangle \tag{A.9}$$

is used to simplified the expression a bit. Which gives

$$E = \frac{C_A^* C_A \langle \psi_A^* | H | \psi_A \rangle + C_A^* C_B \langle \psi_A^* | H | \psi_B \rangle + C_B^* C_B \langle \psi_B^* | H | \psi_B \rangle + C_B^* C_A \langle \psi_B^* | H | \psi_A \rangle}{C_A^* C_A \langle \psi_A^* | \psi_A \rangle + C_A^* C_B \langle \psi_A^* | \psi_B \rangle + C_B^* C_B \langle \psi_B^* | \psi_B \rangle + C_B^* C_A \langle \psi_B^* | \psi_A \rangle} \tag{A.10}$$

The so called overlap integrals are given the following notations

$$\begin{aligned} S_{AA} &= \langle \psi_A^* | \psi_A \rangle , \\ S_{BB} &= \langle \psi_B^* | \psi_B \rangle , \\ S_{AB} &= \langle \psi_A^* | \psi_B \rangle , \\ S_{BA} &= \langle \psi_B^* | \psi_A \rangle . \end{aligned} \tag{A.11}$$

The hopping integrals get the following notations

$$\begin{aligned} H_{AA} &= \langle \psi_A^* | H | \psi_A \rangle \,, \\ H_{BB} &= \langle \psi_B^* | H | \psi_B \rangle \,, \\ H_{AB} &= \langle \psi_A^* | H | \psi_B \rangle \,, \\ H_{BA} &= \langle \psi_B^* | H | \psi_A \rangle = H_{AB}^*. \end{aligned} \tag{A.12}$$

From these notations the expression can be simplified to

$$E = \frac{C_A C_A H_{AA} + C_A C_B H_{AB} + C_B C_B H_{BB} + C_B C_A H_{BA}}{C_A C_A S_{AA} + C_A C_B S_{AB} + C_B C_B S_{BB} + C_B C_A S_{BA}}. \tag{A.13}$$

Moving the denominator of the expression over to the other side, the expression can be written as

$$\begin{aligned} &E(C_A C_A S_{AA} + C_A C_B S_{AB} + C_B C_B S_{BB} + C_B C_A S_{BA}) \\ &= C_A C_A H_{AA} + C_A C_B H_{AB} + C_B C_B H_{BB} + C_B C_A H_{BA}. \end{aligned} \tag{A.14}$$

Which we write in matrix shape to

$$\begin{bmatrix} C_A & C_B \end{bmatrix} \begin{bmatrix} ES_{AA} & ES_{AB} \\ ES_{BA} & ES_{BB} \end{bmatrix} \begin{bmatrix} C_A \\ C_B \end{bmatrix} = \begin{bmatrix} C_A & C_B \end{bmatrix} \begin{bmatrix} H_{AA} & H_{AB} \\ H_{BA} & H_{BB} \end{bmatrix} \begin{bmatrix} C_A \\ C_B \end{bmatrix}$$
$$\begin{bmatrix} C_A & C_B \end{bmatrix} \begin{bmatrix} H_{AA} - ES_{AA} & H_{AB} - ES_{AB} \\ H_{BA} - ES_{BA} & H_{BB} - ES_{BB} \end{bmatrix} \begin{bmatrix} C_A \\ C_B \end{bmatrix} = 0.$$

From this, one can derive the secular determinant

$$\begin{vmatrix} H_{AA} - ES_{AA} & H_{AB} - ES_{AB} \\ H_{BA} - ES_{BA} & H_{BB} - ES_{BB} \end{vmatrix} = 0, \tag{A.15}$$

that becomes

$$(H_{AA} - ES_{AA})(H_{BB} - ES_{BB}) - (H_{AB} - ES_{AB})(H_{BA} - ES_{BA}) = 0. \tag{A.16}$$

Solving for E gives

$$\begin{aligned} E = &- \frac{H_{AB}S_{BA} + H_{BA}S_{AB} - H_{AA}S_{BB} - H_{BB}S_{AA}}{2\left(S_{AA}S_{BB} - S_{AB}S_{BA}\right)} \\ &\pm \sqrt{\frac{H_{AB}S_{BA} + H_{BA}S_{AB} - H_{AA}S_{BB} - H_{BB}S_{AA}}{2\left(S_{AA}S_{BB} - S_{AB}S_{BA}\right)} - H_{AA}H_{BB} + H_{AB}H_{BA}} \end{aligned} \tag{A.17}$$

The assumption that there is no orbital overlap (Huckel approximations) makes

the calculations more manageable [6, 58]. The assumption can be written as

$$\langle \phi^*(\boldsymbol{r}-\boldsymbol{r}_I)|\phi(\boldsymbol{r}-\boldsymbol{r}_J)\rangle = \begin{cases} 0, & \text{if } \boldsymbol{r}_I \neq \boldsymbol{r}_J, \\ 1, & \text{if } \boldsymbol{r}_I = \boldsymbol{r}_J. \end{cases} \tag{A.18}$$

From this assumption the calculation of the overlap integral becomes simpler. S_{AA} in (A.19) still looks very complex. But all terms containing two different lattice point will be zero since there is no orbital overlap, (A.18). On the other hand when a term have the same lattice point, it will remain and add $1/N$ to the total sum. A total of N lattice points means that the value of S_{AA} will be 1, thanks to the normalisation of the wave functions. Note A and A' are in the calculations to make it easier to differentiate, but both are referring to the same atom basis and will be constituted of the same lattice vectors.

$$\begin{aligned}
S_{AA'} &= \int \psi_A^* \psi_{A'}\, d\tau = \frac{1}{N}\sum_A e^{-i\boldsymbol{k}\cdot\boldsymbol{r}_A} \sum_{A'} e^{i\boldsymbol{k}\cdot\boldsymbol{r}_{A'}} \langle \phi^*(\boldsymbol{r}-\boldsymbol{r}_A)|\phi(\boldsymbol{r}-\boldsymbol{r}_{A'})\rangle \\
&= \frac{1}{N} e^{i\boldsymbol{k}\cdot(a_1-\boldsymbol{a}_1)} \langle \phi^*(\boldsymbol{r}-\boldsymbol{a}_1)|\phi(\boldsymbol{r}-\boldsymbol{a}_1)\rangle \\
&\quad + \frac{1}{N} e^{i\boldsymbol{k}\cdot(\boldsymbol{a}_1-\boldsymbol{a}_2)} \langle \phi^*(\boldsymbol{r}-\boldsymbol{a}_2)|\phi(\boldsymbol{r}-\boldsymbol{a}_1)\rangle \\
&\qquad\qquad \vdots \\
&\quad + \frac{1}{N} e^{i\boldsymbol{k}\cdot(\boldsymbol{a}_1-\boldsymbol{a}_N)} \langle \phi^*(\boldsymbol{r}-\boldsymbol{a}_N)|\phi(\boldsymbol{r}-\boldsymbol{a}_1)\rangle \\
&\quad + \frac{1}{N} e^{i\boldsymbol{k}\cdot(\boldsymbol{a}_2-\boldsymbol{a}_1)} \langle \phi^*(\boldsymbol{r}-\boldsymbol{a}_1)|\phi(\boldsymbol{r}-\boldsymbol{a}_2)\rangle \\
&\quad + \frac{1}{N} e^{i\boldsymbol{k}\cdot(\boldsymbol{a}_2-\boldsymbol{a}_2)} \langle \phi^*(\boldsymbol{r}-\boldsymbol{a}_2)|\phi(\boldsymbol{r}-\boldsymbol{a}_2)\rangle \\
&\qquad\qquad \vdots \\
&\quad + \frac{1}{N} e^{i\boldsymbol{k}\cdot(\boldsymbol{a}_2-\boldsymbol{a}_N)} \langle \phi^*(\boldsymbol{r}-\boldsymbol{a}_N)|\phi(\boldsymbol{r}-\boldsymbol{a}_2)\rangle \\
&\qquad\qquad \vdots \\
&\quad + \frac{1}{N} e^{i\boldsymbol{k}\cdot(\boldsymbol{a}_N-\boldsymbol{a}_1)} \langle \phi^*(\boldsymbol{r}-\boldsymbol{a}_1)|\phi(\boldsymbol{r}-\boldsymbol{a}_N)\rangle \\
&\quad + \frac{1}{N} e^{i\boldsymbol{k}\cdot(\boldsymbol{a}_N-\boldsymbol{a}_2)} \langle \phi^*(\boldsymbol{r}-\boldsymbol{a}_2)|\phi(\boldsymbol{r}-\boldsymbol{a}_N)\rangle \\
&\qquad\qquad \vdots \\
&\quad + \frac{1}{N} e^{i\boldsymbol{k}\cdot(\boldsymbol{a}_N-\boldsymbol{a}_N)} \langle \phi^*(\boldsymbol{r}-\boldsymbol{a}_N)|\phi(\boldsymbol{r}-\boldsymbol{a}_N)\rangle \\
&= \frac{1}{N}(e^0 \cdot 1)N = 1
\end{aligned} \tag{A.19}$$

Since the wave functions in graphene are equal, $S_{BB} = S_{AA}$ and therefore

$$S_{BB} = 1. \tag{A.20}$$

Calculating the other overlap integrals in the same manner gives

$$\begin{aligned} S_{AB} &= 0, \\ S_{BA} &= S_{AB} = 0. \end{aligned} \tag{A.21}$$

Now the name "overlap integral" is clarified. When two wave functions do not overlap at all, the value will be zero. On the contrary, if we are looking at two wave functions that completely overlap, in the normalised case, the vale of the overlap integral will be one.

Unfortunately, calculating the hopping integrals is not as easy as calculating the overlap integrals. When calculating the hopping integrals, it is important to know which approximations can be made. A common assumption is that the atoms only interact with their nearest neighbour atoms. But other approximations, such as next-nearest, next-next-nearest neighbour and so on can also be used to get a more precise expression. For simplicity, we start by looking at when atoms are only assumed to interact with their nearest neighbours. This means that

$$\langle \phi^*(\boldsymbol{r} - \boldsymbol{r}_I)|H|\phi(\boldsymbol{r} - \boldsymbol{r}_J)\rangle = \begin{cases} 0, & \text{if } |\boldsymbol{r}_I - \boldsymbol{r}_J| > |\delta_{1,2,3}| \\ > 0, & \text{otherwise} \end{cases} \tag{A.22}$$

The hopping integral H_{AB} can then be calculated as

$$\begin{aligned}
H_{AB} &= \int \psi_A^* H \psi_B \, d\tau = \frac{1}{N} \sum_A e^{-i\boldsymbol{k}\cdot\boldsymbol{r}_A} \sum_B e^{i\boldsymbol{k}\cdot\boldsymbol{r}_B} \langle \phi^*(\boldsymbol{r}-\boldsymbol{r}_A)|H|\phi(\boldsymbol{r}-\boldsymbol{r}_B)\rangle \\
&= \frac{1}{N} e^{i\boldsymbol{k}\cdot(\boldsymbol{b}_1-\boldsymbol{a}_1)} \langle \phi^*(\boldsymbol{r}-\boldsymbol{a}_1)|H|\phi(\boldsymbol{r}-\boldsymbol{b}_1)\rangle \\
&\quad + \frac{1}{N} e^{i\boldsymbol{k}\cdot(\boldsymbol{b}_1-\boldsymbol{a}_2)} \langle \phi^*(\boldsymbol{r}-\boldsymbol{a}_2)|H|\phi(\boldsymbol{r}-\boldsymbol{b}_1)\rangle \\
&\qquad\qquad \vdots \\
&\quad + \frac{1}{N} e^{i\boldsymbol{k}\cdot(\boldsymbol{b}_1-\boldsymbol{a}_N)} \langle \phi^*(\boldsymbol{r}-\boldsymbol{a}_N)|H|\phi(\boldsymbol{r}-\boldsymbol{b}_1)\rangle \\
&\quad + \frac{1}{N} e^{i\boldsymbol{k}\cdot(\boldsymbol{b}_2-\boldsymbol{a}_1)} \langle \phi^*(\boldsymbol{r}-\boldsymbol{a}_1)|H|\phi(\boldsymbol{r}-\boldsymbol{b}_2)\rangle \\
&\quad + \frac{1}{N} e^{i\boldsymbol{k}\cdot(\boldsymbol{b}_2-\boldsymbol{a}_2)} \langle \phi^*(\boldsymbol{r}-\boldsymbol{a}_2)|H|\phi(\boldsymbol{r}-\boldsymbol{b}_2)\rangle \\
&\qquad\qquad \vdots \\
&\quad + \frac{1}{N} e^{i\boldsymbol{k}\cdot(\boldsymbol{b}_2-\boldsymbol{a}_N)} \langle \phi^*(\boldsymbol{r}-\boldsymbol{a}_N)|H|\phi(\boldsymbol{r}-\boldsymbol{b}_2)\rangle \\
&\qquad\qquad \vdots \\
&\quad + \frac{1}{N} e^{i\boldsymbol{k}\cdot(\boldsymbol{b}_N-\boldsymbol{a}_1)} \langle \phi^*(\boldsymbol{r}-\boldsymbol{a}_1)|H|\phi(\boldsymbol{r}-\boldsymbol{b}_N)\rangle \\
&\quad + \frac{1}{N} e^{i\boldsymbol{k}\cdot(\boldsymbol{b}_N-\boldsymbol{a}_2)} \langle \phi^*(\boldsymbol{r}-\boldsymbol{a}_2)|H|\phi(\boldsymbol{r}-\boldsymbol{b}_N)\rangle \\
&\qquad\qquad \vdots \\
&\quad + \frac{1}{N} e^{i\boldsymbol{k}\cdot(\boldsymbol{b}_N-\boldsymbol{a}_N)} \langle \phi^*(\boldsymbol{r}-\boldsymbol{a}_N)|H|\phi(\boldsymbol{r}-\boldsymbol{b}_N)\rangle \,.
\end{aligned} \tag{A.23}$$

The only terms that will remain, is when $\boldsymbol{b}_m - \boldsymbol{a}_n$ is equal to $-\boldsymbol{\delta_1}$, $-\boldsymbol{\delta_2}$ or $-\boldsymbol{\delta_3}$ since that means that the terms are neighbours. The exponential part will be the same for all terms

$$e^{i\boldsymbol{k}\cdot(-\boldsymbol{\delta}_1)} + e^{i\boldsymbol{k}\cdot(-\boldsymbol{\delta}_2)} + e^{i\boldsymbol{k}\cdot(-\boldsymbol{\delta}_3)}. \tag{A.24}$$

When using the fact that $\boldsymbol{k} = (k_x, k_y)$ as well as the values of $\boldsymbol{\delta}_{1,2,3}$ as specified in (2.2), the expression can be written explicitly as

$$\begin{aligned}
f(\boldsymbol{k}) &= e^{ik_x a_{C-C}} + e^{-ia_{C-C}\left(\frac{1}{2}k_x + \frac{\sqrt{3}}{2}k_y\right)} + e^{-ia_{C-C}\left(\frac{1}{2}k_x - \frac{\sqrt{3}}{2}k_y\right)} \\
&= e^{ik_x a_{C-C}} + 2\cos\left(\frac{\sqrt{3}}{2}k_y a_{C-C}\right) e^{-i\frac{1}{2}k_x a_{C-C}}.
\end{aligned} \tag{A.25}$$

The other part of H_{AB} we define as

$$h_0 = \frac{1}{N}\sum_A \sum_B \langle \phi_A^*(\boldsymbol{r}-\boldsymbol{r}_A)|H|\phi_B(\boldsymbol{r}-\boldsymbol{r}_B)\rangle \tag{A.26}$$

for all A and B where $|b_m - a_n| = |\boldsymbol{\delta}_{1,2,3}|$. This gives us a simpler expression

$$H_{AB} = f(\boldsymbol{k})h_0, \tag{A.27}$$

where the first part is known. Calculating H_{BA} can be done in the same manner and will show that

$$H_{BA} = H_{AB}^*, \tag{A.28}$$

which will prove useful for us. Next, we take a look at the hopping integrals for the same sublattices. Starting off with $H_{AA'}$. Note that the use of the notation A and A' are used even though they represent the same sublattice. Since we have made the assumption that atoms only interact with their nearest neighbour atoms, the hopping integral will be zero unless it is the same lattice vector in the term. This means that we can simplify the expression as follows

$$\begin{aligned} H_{AA} &= \int \psi_A^* H \psi_{A'}\, d\tau = \frac{1}{N}\sum_A e^{-i\boldsymbol{k}\cdot\boldsymbol{r}_A}\sum_{A'} e^{i\boldsymbol{k}\cdot\boldsymbol{r}_{A'}}\,\langle \phi^*(\boldsymbol{r}-\boldsymbol{r}_A)|H|\phi(\boldsymbol{r}-\boldsymbol{r}_{A'})\rangle \\ &= \frac{1}{N}e^0\sum_A \langle \phi^*(\boldsymbol{r}-\boldsymbol{r}_A)|H|\phi(\boldsymbol{r}-\boldsymbol{r}_A)\rangle\,. \end{aligned} \tag{A.29}$$

The value is sometimes written as $H_{AA} = E_{2p}$. Using the same method, the expression of H_{BB} can be found. Since the two different subsets of lattices all have the same atoms

$$H_{AA} = H_{BB} = E_{2p}. \tag{A.30}$$

The expression for the energy dispersion is now somewhat simplified as

$$\begin{aligned} E &= E_{2p} \pm \sqrt{-E_{2p} - E_{2p}E_{2p} + f(\boldsymbol{k})h_0(f(\boldsymbol{k})h_0)^*} \\ &= E_{2p} \pm \sqrt{|f(\boldsymbol{k})h_0|^2 - E_{2p}(1+E_{2p})}. \end{aligned} \tag{A.31}$$

The positive part of the energy dispersion refers to the conduction band and the negative part to the valence band. In calculations, one often consider $E_{2p} = 0$, to centre the band structure around zero, [6, 19] this further simplifies the expression

$$E = \pm h_0\sqrt{|f(\boldsymbol{k})|^2}. \tag{A.32}$$

We already know the value of $|f(\boldsymbol{k})|^2$, which can be simplified as

$$\begin{aligned}
|f(\boldsymbol{k})|^2 &= f^*(\boldsymbol{k})f(\boldsymbol{k}) \\
&= \left(e^{-ik_x a_{C-C}} + e^{ia_{C-C}\left(\frac{1}{2}k_x + \frac{\sqrt{3}}{2}k_y\right)} + e^{ia_{C-C}\left(\frac{1}{2}k_x - \frac{\sqrt{3}}{2}k_y\right)}\right) \\
&\quad \cdot \left(e^{ik_x a_{C-C}} + e^{-ia_{C-C}\left(\frac{1}{2}k_x + \frac{\sqrt{3}}{2}k_y\right)} + e^{-ia_{C-C}\left(\frac{1}{2}k_x - \frac{\sqrt{3}}{2}k_y\right)}\right) \\
&= 3 + 4\cos\left(\frac{\sqrt{3}}{2}k_y a_{C-C}\right)\cos\left(\frac{3}{2}k_x a_{C-C}\right) + 2\cos\left(\sqrt{3}k_y a_{C-C}\right).
\end{aligned} \tag{A.33}$$

Using the same method and technique, while instead approximating so that the orbitals interact also with their next-nearest neighbours. The energy dispersion for this approximation can be written as

$$E_{\pm}(\boldsymbol{k}) = \pm\, h_0\sqrt{|f(\boldsymbol{k})|^2} - h_1|f(\boldsymbol{k})|^2, \tag{A.34}$$

where h_0 is the hopping integral as described earlier and h_1 is the next-nearest neighbour hopping energy defined as

$$h_1 = \frac{1}{N}\sum_A \sum_B \langle \phi_A^*(\boldsymbol{r} - \boldsymbol{r}_A)|H|\phi_B(\boldsymbol{r} - \boldsymbol{r}_B)\rangle \tag{A.35}$$

for all A and B where $|\boldsymbol{b}_m - \boldsymbol{a}_n| = |\boldsymbol{\delta}_{1',2',3',4',5',6'}|$ [19, 58].

Appendix B

Weyl Hamiltonian for graphene

Equation 2.9 describes the dispersion relation in graphene near the K-points, the equation is shown figure 2.9 as L and R. Even though (2.9) is often referred to as being linear, $|\boldsymbol{k}|$ does not necessarily have to be linear. For example, if $\boldsymbol{k} = (k_x, k_y)$, the energy dispersion is

$$E\psi = \pm\hbar v_F \sqrt{{k_x}^2 + {k_y}^2} \tag{B.1}$$

which is not linear. But with some small tricks the useful Weyl Hamiltonian for graphene can be derived. Firstly, using the deBroglie relationship

$$\boldsymbol{p} = \hbar\boldsymbol{k}, \tag{B.2}$$

the expression for E can be re-written as

$$E\psi = \pm v_F \sqrt{(\hbar k_x)^2 + (\hbar k_y)^2}\psi = \pm v_F \sqrt{(p_x)^2 + (p_y)^2}\psi. \tag{B.3}$$

Next, using the following relationship

$$\boldsymbol{p} = -i\hbar\boldsymbol{\nabla}, \tag{B.4}$$

the expression can be written as

$$\begin{aligned} E\psi &= \pm v_F \sqrt{(-1)^2 i^2 \hbar^2 \nabla^2}\psi = \pm\hbar v_F \sqrt{-\nabla^2}\psi, \\ &= \pm i\hbar v_F \sqrt{\nabla^2}\psi. \end{aligned} \tag{B.5}$$

Here we can see that we need to take the square root of the Laplacian operator, which makes the problem less trivial than it first appeared. But with the help of Pythagoras theorem, the absolute value of $\boldsymbol{k}$ can be written in a different manner.

$$k^2 = {k_x}^2 + {k_y}^2, \tag{B.6}$$

together with a re-write version of $\boldsymbol{k}$ as a linear function

$$|\boldsymbol{k}| = k = \sigma_x k_x + \sigma_y k_y. \tag{B.7}$$

From this a relationship between $\boldsymbol{\sigma}$ and $\boldsymbol{k}$ can be expressed such as

$$\begin{aligned}
k &= \sigma_x k_x + \sigma_y k_y \\
&\Leftrightarrow \\
k^2 &= (\sigma_x k_x + \sigma_y k_y)^2 \\
&\Leftrightarrow \\
{k_x}^2 + {k_y}^2 &= \sigma_x^2 {k_x}^2 + (\sigma_x\sigma_y + \sigma_y\sigma_x)k_x k_y + \sigma_y^2 {k_y}^2 \\
&\Leftrightarrow \\
&\begin{cases}
\sigma_x^2 & = 1 \\
\sigma_y^2 & = 1 \\
\sigma_x\sigma_y + \sigma_y\sigma_x & = 0.
\end{cases}
\end{aligned} \tag{B.8}$$

A re-write of (B.5), using equations (B.2) and (B.4) as well and the notation $\boldsymbol{\sigma} = (\sigma_x, \sigma_y)$ gives [29]

$$E\psi = \pm i\hbar v_F \boldsymbol{\sigma}\cdot\boldsymbol{k} = \pm i v_F \boldsymbol{\sigma}\cdot\boldsymbol{p} = \pm v_F \boldsymbol{\sigma}\cdot(-i\hbar\boldsymbol{\nabla}) \tag{B.9}$$

Which is how we get the Hamiltonian for massless Dirac particles, the so called Weyl Hamiltonian [59]

$$H = -i\hbar v_F \boldsymbol{\sigma}\cdot\boldsymbol{\nabla}, \tag{B.10}$$

commonly used in research literature [29].

$$E\psi = \pm i\hbar v_F \left(\sigma_x \frac{\delta}{\delta x} + \sigma_y \frac{\delta}{\delta y}\right)\psi. \tag{B.11}$$

Bibliography

[1] F. Schwierz, "Graphene transistors: status, prospects, and problems," *Proc. IEEE*, vol. 101, no. 7, pp. 1567–1584, May 2013. [Online]. Available: http://ieeexplore.ieee.org/document/6518205/ [Accessed: 03-Oct-2016].

[2] C. Pugnaghi *et al.*, "Semianalytical quantum model for graphene field-effect transistors," *J. Appl. Phys.*, vol. 116, no. 114505, pp. 1–9, 2014. [Online]. Available: http://scitation.aip.org/content/aip/journal/jap/116/11/10.1063/1.4895993 [Accessed: 04-Oct-2016].

[3] A. C. Ferrari *et al.*, "Science and technology roadmap for graphene, related two-dimensional crystals, and hybrid systems," *Nanoscale*, vol. 7, no. 11, pp. 4598–4810, 2015. [Online]. Available: http://dx.doi.org/10.1039/C4NR01600A [Accessed: 11-Oct-2016].

[4] S. Rakheja *et al.*, "A unified charge-current compact model for ambipolar operation in quasi-ballistic graphene transistors: Experimental verification and circuit-analysis demonstration," in *2013 IEEE International Electron Devices Meeting*. Washington, DC, USA: IEEE, Dec. 2013, pp. 5.5.1–5.5.4. [Online]. Available: http://ieeexplore.ieee.org/document/6724568/ [Accessed: 15-Nov-2016].

[5] J. Handy, "How many transistors have ever shipped?" *Forbes*, 2014. [Online]. Available: https://www.forbes.com/sites/jimhandy/2014/05/26/how-many-transistors-have-ever-shipped/#2a03e9c04425 [Accessed: 29-Oct-2016].

[6] A. H. Castro Neto, F. Guinea, N. M. R. Peres, K. S. Novoselov, and A. K. Geim, "The electronic properties of graphene," *Rev. Mod. Phys.*, vol. 81, no. 1, p. 109, 2009. [Online]. Available: http://link.aps.org/doi/10.1103/RevModPhys.81.109 [Accessed: 7-Oct-2016].

[7] W. Liu, *Fundamentals of III-V Devices: HBTs, MESFETs, and HFETs/HEMTs*. New York: John Wiley & Sons Inc., 1999.

[8] M. I. Katsnelson, K. S. Novoselov, and A. K. Geim, "Chiral tunnelling and the klein paradox in graphene," *Nature Phys.*, vol. 2, no. 9, pp. 620–625, 2006. [Online]. Available: http://www.nature.com/nphys/journal/v2/n9/suppinfo/nphys384_S1.html [Accessed: 31-Oct-2016].

[9] D. Dragoman and M. Dragoman, "Negative differential resistance of electrons in graphene barrier," *Appl. Phys. Lett.*, vol. 90, no. 14, pp. 143 111–1–143 111–3, 2007. [Online]. Available: http://scitation.aip.org/content/aip/journal/apl/90/14/10.1063/1.2719670 [Accessed: 27-Oct-2016].

[10] M. I. Katsnelson, "Graphene: carbon in two dimensions," *Mater. Today*, vol. 10, no. 1–2, pp. 20–27, 2007. [Online]. Available: http://www.sciencedirect.com/science/article/pii/S1369702106717886 [Accessed: 31-Oct-2016].

[11] G. E. Moore, "Cramming more components onto integrated circuits," *Electronics*, vol. 38, no. 8, Apr. 1965.

[12] G. E. Moore, "No exponential is forever: but "forever" can be delayed!" in *Solid-State Circuits Conference, 2003. Digest of Technical Papers. ISSCC. 2003 IEEE International*. IEEE, 2003, pp. 20–23. [Online]. Available: http://ieeexplore.ieee.org/document/1234194 [Accessed: 03-Oct-2016].

[13] M. C. Lemme, T. J. Echtermeyer, M. Baus, and H. Kurz, "A graphene field-effect device," *IEEE Electron Device Lett.*, vol. 28, no. 4, pp. 282–284, apr 2007. [Online]. Available: http://ieeexplore.ieee.org/document/4137639/ [Accessed: 09-Jan-2017].

[14] J. Tian, A. Katsounaros, D. Smith, and Y. Hao, "Graphene field-effect transistor model with improved carrier mobility analysis," *IEEE Trans. Electron Devices*, vol. 62, no. 10, pp. 3433–3440, 2015. [Online]. Available: http://ieeexplore.ieee.org/document/7230253/ [Accessed: 03-Oct-2016].

[15] G. M. Landauer, D. Jimenez, and J. L. González, "An accurate and verilog-a compatible compact model for graphene field-effect transistors," *IEEE Trans. Nanotechnol.*, vol. 13, no. 5, pp. 895–904, 2014. [Online]. Available: http://ieeexplore.ieee.org/document/6825842/ [Accessed: 25-Oct-2016].

[16] D. Jimenez and O. Moldovan, "Explicit drain-current model of graphene field-effect transistors targeting analog and radio-frequency applications,"

IEEE Trans. Electron Devices, vol. 58, no. 11, pp. 4049–4052, 2011. [Online]. Available: http://ieeexplore.ieee.org/abstract/document/6018290/ [Accessed: 25-Oct-2016].

[17] "Advanced design system (ads) 2016.01," Keysight Technologies, Santa Rosa, CA, United States, 2016. [Online]. Available: http://www.keysight.com/en/pc-1297113/advanced-design-system

[18] "Matlab version 9.0.0.341360 (r2016a)," The Mathworks, Inc., Natick, Massachusetts, United States, 2016. [Online]. Available: http://www.mathworks.com/products/matlab/

[19] M. Andersson, "Characterisation and modelling of graphene FETs for terahertz mixers and detectors," Ph.D. dissertation, Chalmers University of Technology, Gothenburg, 2016.

[20] D. Reddy, L. F. Register, G. D. Carpenter, and S. K. Banerjee, "Graphene field-effect transistors," *J. Phys. D: Appl. Phys.*, vol. 44, no. 31, pp. 1–20, 2011. [Online]. Available: http://stacks.iop.org/0022-3727/44/i=31/a=313001 [Accessed: 26-Oct-2016].

[21] P. R. Wallace, "The band theory of graphite," *Phys. Rev.*, vol. 71, pp. 622–634, May 1947. [Online]. Available: http://link.aps.org/doi/10.1103/PhysRev.71.622 [Accessed: 3-Feb-2017].

[22] R. J. Tilley, *Crystals and crystal structures.* John Wiley & Sons, 2006.

[23] W. Setyawan and S. Curtarolo, "High-throughput electronic band structure calculations: Challenges and tools," *Comput. Mater. Sci.*, vol. 49, no. 2, pp. 299 – 312, 2010. [Online]. Available: http://www.sciencedirect.com/science/article/pii/S0927025610002697 [Accessed: 5-Dec-2016].

[24] V. Nam Do, V. Nguyen Hung, P. Dollfus, and A. Bournel, "Electronic transport and spin-polarization effects of relativisticlike particles in mesoscopic graphene structures," *J. Appl. Phys.*, vol. 104, no. 6, pp. 063 708–1–063 708–7, 2008. [Online]. Available: http://scitation.aip.org/content/aip/journal/jap/104/6/10.1063/1.2980045 [Accessed: 28-Oct-2016].

[25] A. Mangla, "Modeling nanoscale quasi-ballistic MOS transistors: a circuit design perspective," Ph.D. dissertation, École Polytechnique Fédérale de Lausanne, Lausanne, 2014. [Online]. Available: https://infoscience.epfl.ch/record/203255/files/EPFL_TH6385.pdf [Accessed: 14-Oct-2016].

[26] M. O. Goerbig, "Electronic properties of graphene in a strong magnetic field," *Rev. Mod. Phys.*, vol. 83, no. 4, p. 1193, 2011. [Online]. Available: http://journals.aps.org/rmp/abstract/10.1103/RevModPhys.83.1193 [Accessed: 23-Feb-2017].

[27] C. González, J. Ruiz, R. Bonilla, and A. Ávila, "Quantum tunnelling demonstration using a low-cost experimental setup," in *Micro-Nanoelectronics, Technology and Applications (*EAMTA*), 2013 7th Argentine School of Micro-Nanoelectronics, Technology and Applications*. IEEE, 2013, pp. 78–85. [Online]. Available: http://ieeexplore.ieee.org/abstract/document/6621082/ [Accessed: 2-Mar-2017].

[28] O. Klein, "Die reflexion von elektronen an einem potentialsprung nach der relativistischen dynamik von dirac," *Zeitschrift für Physik*, vol. 53, no. 3, pp. 157–165, 1929. [Online]. Available: https://link.springer.com/article/10.1007%2FBF01339716 [Accessed: 9-Mar-2017].

[29] T. Robinson, "On klein tunneling in graphene," *Am. J. Phys.*, vol. 80, no. 2, pp. 141–147, 2012.

[30] N. Dombey and A. Calogeracos, "Seventy years of the klein paradox," *Phys. Rep.*, vol. 315, no. 1, pp. 41–58, 1999. [Online]. Available: http://www.sciencedirect.com/science/article/pii/S037015739900023X [Accessed: 9-Mar-2017].

[31] H. Hai, F. Xing-Qiu, and H. Rong-Sheng, "Klein paradox of two-dimensional dirac electrons in circular well potential," *Commun. Theor. Phys.*, vol. 58, no. 2, p. 205–208, 2010. [Online]. Available: http://stacks.iop.org/0253-6102/58/i=2/a=06 [Accessed: 9-Mar-2017].

[32] H. Wang, A. Hsu, J. Kong, D. A. Antoniadis, and T. Palacios, "Compact virtual-source current-voltage model for top-and back-gated graphene field-effect transistors," *IEEE Trans. Electron Devices*, vol. 58, no. 5, pp. 1523–1533, 2011. [Online]. Available: http://ieeexplore.ieee.org/document/5735198/ [Accessed: 31-Oct-2016].

[33] Y.-S. Woo, S.-A. Seo, D.-C. Kim, and H.-J. Chung, "Electronic device using a two-dimensional sheet material, transparent display and methods of fabricating the same," U.S. Patent 8 513 653, aug, 2013. [Online]. Available: https://www.google.co.uk/patents/US8513653 [Accessed: 13-Oct-2016].

[34] C. News, "Columbia engineers prove graphene is the strongest material," *Columbia News*, 2008. [Online]. Available: http://www.columbia.edu/cu/news/08/07/graphene.html [Accessed: 09-Mar-2017].

[35] S. Mirsky, "Elephant illustrates important point," *Sci. Am.*, 2011. [Online]. Available: https://www.scientificamerican.com/article/balancing-act/ [Accessed: 10-Mar-2017].

[36] E. H. Hwang and S. Das Sarma, "Acoustic phonon scattering limited carrier mobility in two-dimensional extrinsic graphene," *Phys. Rev. B*, vol. 77, p. 115449, Mar 2008. [Online]. Available: https://link.aps.org/doi/10.1103/PhysRevB.77.115449 [Accessed: 31-Oct-2016].

[37] K. Bolotin *et al.*, "Ultrahigh electron mobility in suspended graphene," *Solid State Commun.*, vol. 146, no. 9–10, pp. 351 – 355, 2008. [Online]. Available: http://www.sciencedirect.com/science/article/pii/S0038109808001178 [Accessed: 31-Oct-2016].

[38] P. Sharma, L. S. Bernard, A. Bazigos, A. Magrez, and A. M. Ionescu, "Room-temperature negative differential resistance in graphene field effect transistors: Experiments and theory," *ACS Nano*, vol. 9, no. 1, pp. 620–625, 2015. [Online]. Available: http://dx.doi.org/10.1021/nn5059437 [Accessed: 28-Oct-2016].

[39] H. Bennett *et al.*, "International technology roadmap for semiconductors 2.0 - 2015 edition - beyond CMOS," 2015. [Online]. Available: http://www.semiconductors.org/clientuploads/Research_Technology/ITRS/2015/6_2015%20ITRS%202.0%20Beyond%20CMOS.pdf [Accessed: 1-Jan-2017].

[40] A. K. Geim and K. S. Novoselov, "The rise of graphene," *Nat. Mater.*, vol. 6, no. 3, pp. 183–191, 2007. [Online]. Available: http://www.nature.com/nmat/journal/v6/n3/abs/nmat1849.html [Accessed: 7-Jan-2017].

[41] W. Shockley, "A unipolar "field-effect" transistor," *Proc. IRE*, vol. 40, no. 11, pp. 1365–1376, nov 1952. [Online]. Available: http://ieeexplore.ieee.org/document/4050836/ [Accessed: 29-Oct-2016].

[42] S.-L. Li, H. Miyazaki, A. Kumatani, A. Kanda, and K. Tsukagoshi, "Low operating bias and matched input- output characteristics in graphene logic inverters," *Nano Lett.*, vol. 10, no. 7, pp. 2357–2362, 2010. [Online]. Available: http://pubs.acs.org/doi/abs/10.1021/nl100031x [Accessed: 24-Mar-20170].

[43] R. Cheng *et al.*, "High-frequency self-aligned graphene transistors with transferred gate stacks," *Proc. Natl. Acad. Sci. U.S.A.*, vol. 109, no. 29, pp. 11 588–11 592, 2012. [Online]. Available: http://www.pnas.org/content/109/29/11588 [Accessed: 11-Jan-2017].

[44] F. Schwierz, "Graphene transistors," *Nat. Nanotech.*, vol. 5, no. 7, pp. 487–496, 2010. [Online]. Available: http://www.nature.com/nnano/journal/v5/n7/full/nnano.2010.89.html [Accessed: 3-Nov-2016].

[45] S. A. Thiele, J. A. Schaefer, and F. Schwierz, "Modeling of graphene metal-oxide-semiconductor field-effect transistors with gapless large-area graphene channels," *J. Appl. Phys.*, vol. 107, no. 9, pp. 094 505–1–094 505–8, 2010. [Online]. Available: http://aip.scitation.org/doi/10.1063/1.3357398 [Accessed: 17-Jan-2017].

[46] R. Yan *et al.*, "Determination of graphene work function and graphene-insulator-semiconductor band alignment by internal photoemission spectroscopy," *Appl. Phys. Lett.*, vol. 101, no. 2, pp. 022 105–1–022 105–4, 2012. [Online]. Available: http://aip.scitation.org/doi/10.1063/1.4734955 [Accessed: 11-Jan-2017].

[47] D. Jimenez, "Explicit drain current, charge and capacitance model of graphene field-effect transistors," *IEEE Trans. Electron Devices*, vol. 58, no. 12, pp. 4377–4383, dec 2011. [Online]. Available: http://ieeexplore.ieee.org/document/6054021/ [Accessed: 21-Nov-2016].

[48] S. Rakheja *et al.*, "An ambipolar virtual-source-based charge-current compact model for nanoscale graphene transistors," *IEEE Trans. Nanotechnol.*, vol. 13, no. 5, pp. 1005–1013, 2014. [Online]. Available: http://ieeexplore.ieee.org/document/6868269/ [Accessed: 15-Nov-2016].

[49] T. Fang, A. Konar, H. Xing, and D. Jena, "Carrier statistics and quantum capacitance of graphene sheets and ribbons," *Appl. Phys. Lett.*, vol. 91, no. 9, pp. 092 109–1–092 109–3, aug 2007. [Online]. Available: http://scitation.aip.org/content/aip/journal/apl/91/9/10.1063/1.2776887 [Accessed: 7-Nov-2016].

[50] Y. Wu *et al.*, "Three-terminal graphene negative differential resistance devices," *ACS Nano*, vol. 6, no. 3, pp. 2610–2616, 2012. [Online]. Available: http://dx.doi.org/10.1021/nn205106z [Accessed: 27-Oct-2016].

[51] K. N. Parrish, M. E. Ramón, S. K. Banerjee, and D. Akinwande, "A compact model for graphene fets for linear and non-linear circuits," in *IEEE*

17th International Conference on Simulation of Semiconductor Processes and Devices, Denver, CO, USA, 2012, pp. 75–78.

[52] A. Mangla, J.-M. Sallese, C. Sampedro, F. Gamiz, and C. Enz, "Role of the gate in ballistic nanowire SOI MOSFETs," *Solid-State Electron.*, vol. 112, pp. 24–28, 2015. [Online]. Available: http://www.sciencedirect.com/science/article/pii/S0038110115000556 [Accessed: 24-Oct-2016].

[53] A. Mangla, J.-M. Sallese, C. Sampedro, F. Gamiz, and C. Enz, "Modeling the channel charge and potential in quasi-ballistic nanoscale double-gate MOSFETs," *IEEE Trans. Electron Devices*, vol. 61, no. 8, pp. 2640–2646, 2014. [Online]. Available: http://ieeexplore.ieee.org/document/6832484/ [Accessed: 18-Oct-2016].

[54] E. Gnani, A. Gnudi, S. Reggiani, and G. Baccarani, "Quasi-ballistic transport in nanowire field-effect transistors," *IEEE Trans. Electron Devices*, vol. 55, no. 11, pp. 2918–2930, 2008. [Online]. Available: http://ieeexplore.ieee.org/document/4648223/ [Accessed: 26-Oct-2016].

[55] V. E. Dorgan, M.-H. Bae, and E. Pop, "Mobility and saturation velocity in graphene on sio2," *Appl. Phys. Lett.*, vol. 97, no. 8, pp. 082 112–1–082 112–3, 2010. [Online]. Available: http://dx.doi.org/10.1063/1.3483130 [Accessed: 13-Feb-2017].

[56] I. Meric *et al.*, "Current saturation in zero-bandgap, top-gated graphene field-effect transistors," *Nat. Nanotech.*, vol. 3, no. 11, pp. 654–659, 2008. [Online]. Available: http://www.nature.com/nnano/journal/v3/n11/full/nnano.2008.268.html [Accessed: 3-Nov-2016].

[57] S. Thiele and F. Schwierz, "Modeling of the steady state characteristics of large-area graphene field-effect transistors," *J. Appl. Phys.*, vol. 110, no. 3, p. 034506, 2011. [Online]. Available: http://aip.scitation.org/doi/10.1063/1.3606583 [Accessed: 3-Nov-2016].

[58] P. A. M. Dirac, *The principles of quantum mechanics*, 3rd ed. Clarendon Press, 1974.

[59] L. Lu *et al.*, "Experimental observation of weyl points," *Science*, vol. 349, no. 6248, pp. 622–624, 2015. [Online]. Available: http://science.sciencemag.org/content/349/6248/622 [Accessed: 9-Mar-2017].